Aerosol Optical Properties and Particle Size Distributions on the East Coast of the United States Derived from Airborne In Situ and Remote Sensing Measurements

DAVID R. REIDMILLER AND PETER V. HOBBS

Department of Atmospheric Sciences, University of Washington, Seattle, Washington

RALPH KAHN

Jet Propulsion Laboratory, Pasadena, California

ABSTRACT

Airborne in situ measurements of vertical profiles and horizontal transects of aerosol optical and physical properties, obtained during the Chesapeake Lighthouse and Aircraft Measurements for Satellites (CLAMS) field campaign off the East Coast of the United States during the summer of 2001, are presented. Most of the measurements were obtained in relatively clean air dominated by airflows that had passed over Canada and the northern Atlantic Ocean. Results from the 17 July and 2 August 2001 flights are presented; on these days, the aerosol loading was relatively high. In the lower troposphere, ω_0 values at a wavelength of 550 nm were consistently above 0.93 throughout the field experiment, indicating the dominance of weakly absorbing aerosol. Particle number size distributions are presented and discussed for transects at altitudes ~0.05–3.5 km above mean sea level. Particles with diameters (D_p) <0.1 μm made up the majority of the aerosol number. Accumulation mode particles dominate the number size, surface area, and volume distributions. The variability of optical and physical aerosol parameters was analyzed on horizontal scales of ~1–4 km. There was little horizontal variability in the single-scattering albedo (ω_0), aerosol optical depth (AOD), and accumulation mode size, but greater variability in particle number concentration. Comparisons of the airborne measurements with remotely sensed aerosol parameters, such as ω_0 and effective particle radius (r_{eff}), derived from the Multiangle Imaging Spectroradiometer (MISR) aboard the *Terra* satellite were generally in good agreement. Overall, the MISR retrievals captured both the similarities and the differences between the properties of the aerosols measured on 17 July and 2 August.

1. Introduction

Anthropogenic aerosols play an important role in attenuating solar radiation as it passes through the atmosphere, which in turn affects the temperature of the earth (Houghton et al. 2001). The amount of attenuation depends on several factors, including the particle light scattering and light absorption coefficients (σ_{sp} and σ_{ap}, respectively), single-scattering albedo (ω_0), particle number concentrations, and particle size distributions.

Within the past decade, technological advancements have made possible satellite instruments capable of remotely measuring various aerosol parameters. The Multiangle Imaging Spectroradiometer (MISR) is one such instrument currently orbiting Earth on the NASA Earth Observing System's (EOS) *Terra* satellite (Diner et al. 1998). MISR has the potential to provide detailed information on aerosol properties worldwide (Kahn et al. 1998, 2001; Martonchik et al. 1998). However, as with any new remote sensing instrument, it requires in situ data to validate and refine its retrievals.

The Chesapeake Lighthouse and Aircraft Measurements for Satellites (CLAMS) campaign was designed for the purpose of validating NASA EOS *Terra* data products (Smith et al. 2005). CLAMS was carried out from 10 July to 2 August 2001 off the East Coast of the United States. This campaign involved several research aircraft, including the University of Washington's (UW) Convair-580 and National Aeronautic and Space Administration (NASA)'s ER-2 aircraft. Here, we discuss only the in situ measurements collected by the Convair-580 and the remotely sensed MISR aerosol retrievals. The objectives of this paper are: 1) to provide

Corresponding author address: David R. Reidmiller, Dept. of Atmospheric Sciences, University of Washington, Box 351640, Seattle, WA 98195-1640.
E-mail: dreidm@atmos.washington.edu

TABLE 1. Flight dates, UW flight numbers, times, and locations along with relevant MISR/*Terra* overpasses for the 11 flights in which the Convair-580 collected data during CLAMS. An asterisk (*) indicates Convair-580 flight data analyzed in this paper.

Date (2001)	UW flight number	Period of flight (UTC)	Principal locations	*Terra* (MISR) overpass
10 Jul	1870	1725–2220	Near Chesapeake Bay Lighthouse	1602 UTC (Convair-580 take-off delayed; overpass missed)
12 Jul	1871	1102–1640	Near Chesapeake Bay Lighthouse	N/A
14 Jul	1872	1433–1749	Near Chesapeake Bay Lighthouse	N/A
16 Jul	1873	1630–1947	Near Chesapeake Bay Lighthouse and buoys 44014 and 41001	N/A
17 Jul	1874*	1228–1816	1) Near Chesapeake Bay Lighthouse 2) Great Dismal Swamp	1608 UTC
23 Jul	1875	1351–1646	~70 miles east of Wallops Flight Center	N/A
26 Jul	1879	1528–1909	1) Chesapeake Bay Lighthouse 2) Buoy 44014	1607 UTC (cloudy skies)
30 Jul	1879	1609–1951	1) Chesapeake Bay Lighthouse 2) Buoy 44014	N/A
31 Jul	1880	1424–2004	1) Buoy 44004 2) From buoy 44004 to Great Dismal Swamp via Chesapeake Bay Lighthouse	N/A
2 Aug	1881*	1521–1859	1) Chesapeake Bay Lighthouse 2) Buoy 44014 3) 60 miles east of Wallops Flight Center	1608 UTC
2 Aug	1882	1914–2042	Chesapeake Bay Lighthouse	N/A

a general characterization of the optical properties and size distributions of the aerosol sampled during CLAMS. 2) To analyze small-scale horizontal variability in particle light scattering coefficient (σ_{sp}), particle light absorption coefficient (σ_{ap}), single-scattering albedo (ω_0), accumulation, and coarse mode size parameters, total particle number concentration (N) and aerosol optical depth (AOD). 3) To compare aerosol properties derived from airborne in situ measurements with those from remotely sensed MISR retrievals. Smith et al. (2005) present a thorough discussion of the CLAMS field campaign, its objectives, platforms and instrumentation, and some preliminary results. Magi et al. (2005) and Castanho et al. (2005) discuss chemical composition and apportionment of CLAMS aerosol optical depth (AOD), as measured aboard the Convair-580. Redemann et al. (2005) describe the horizontal variability of AOD in CLAMS, based on 14-channel Ames Airborne Tracking Sunphotometer (AATS-14) observations.

This paper is organized as follows: section 2 discusses the Convair-580 aerosol measurements used in this study, their uncertainties, and the MISR products to which they are compared, section 3a covers the particle properties derived from the Convair-580 instruments, section 3b discusses their variability, and section 3c presents a critical comparison between the Convair-580 and MISR results. A summary and conclusions are given in section 4.

2. Instrumentation and methodology

Table 1 lists the dates and times of all the Convair-580 aircraft's flights, as well as the times of the *Terra* overpasses. On three occasions (17 July, 26 July, and 2 August), the Convair-580 underflew the *Terra* satellite. Since 26 July was cloudy, making it difficult for passive remote sensing instruments such as MISR to perform aerosol retrievals, measurements obtained on 17 July and 2 August under generally cloud-free skies, are discussed in this paper.

Typical Convair-580 flight patterns during CLAMS are shown in Figs. 1a,b. These figures illustrate time/height cross sections for the CLAMS flight on 17 July and for the 2 August 2001 flight, respectively. Convair-580 flight patterns generally consisted of several horizontal transects ranging in altitude from ~0.05 to ~3.5 km above mean sea level (MSL) and several vertical profiles, as shown in Figs. 1a,b. Each transect was flown for up to 45 min, with continuous measurements being made. Along-wind and crosswind legs were flown to measure horizontal variability. Table 2 provides details on the vertical profiles and horizontal transects for the two flights of interest here.

Except for surface temperature and pressure, all of the suborbital measurements presented in this paper were obtained aboard the UW Convair-580 research aircraft. The aerosol instruments were located on two interior aircraft racks and under the left wing of the
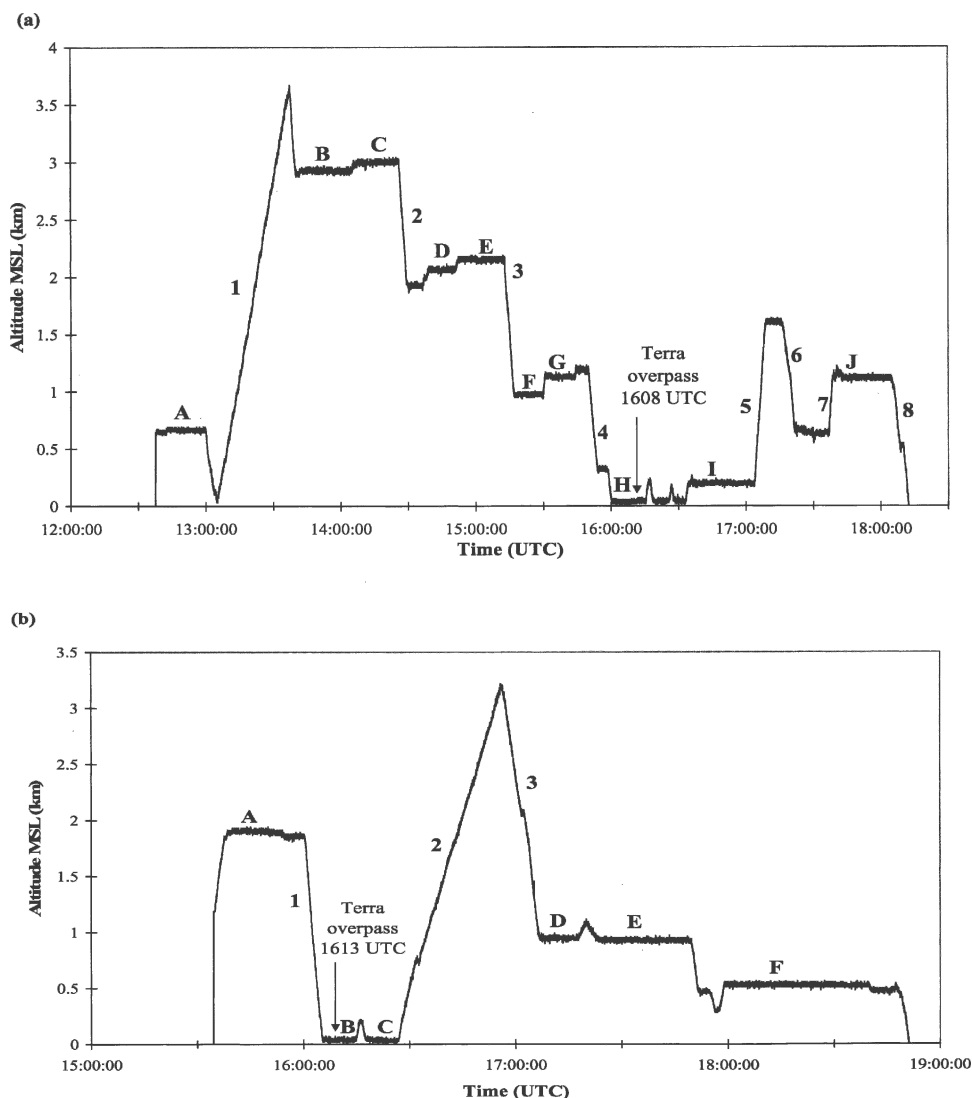
FIG. 1. Time–height cross section for (a) the 17 Jul 2001 Convair-580 flight and (b) the 2 Aug 2001 flight. The aircraft altitude was derived from the hypsometric equation. Note the *Terra* (MISR) overpass during transect H at 1608 UTC in (a) and during transect B at 1608 UTC in (b).

aircraft and sampled from a continuous airstream (the equivalent of ambient air). An important objective of CLAMS was to provide height-resolved aerosol properties as validation data against which to test the remotely sensed aerosol parameters derived from MISR. Therefore, it is of extreme importance to ensure the Convair-580 instruments were calibrated accurately. In the remainder of this section we describe the calibration procedures for the instruments aboard the Convair-580 that are used in this paper.

a. State parameters

Aircraft location was determined using an onboard global positioning system (GPS). Magi et al. (2005) ex-

plain how aircraft altitude was calculated hypsometrically. The altitudes given in this paper are measured from MSL.

Ambient pressure was measured onboard with a Rosemount 830BA barometer (range: 1100–150 hPa). Ambient temperature was measured with a UW-manufactured reverse-flow thermometer (range: $-60°$ to $40°C$), and in-flight relative humidity (RH) was measured with an Ophir Model IR-2000 optical hygrometer. Mean (with one standard deviation) and maximum RH values for each profile and transect of both flights are reported in Table 2. The Rosemount barometer and the reverse-flow thermometer were calibrated prior to CLAMS (on 17 April 2001) with measurements

TABLE 2. Description of the 17 Jul and 2 Aug Convair-580 flights during CLAMS. Each flight consisted of a series of vertical profiles and horizontal transects at various altitudes ranging from sea level (~50 m MSL) to ~3.5 km MSL. Zonal and meridional coordinates of the aircraft were determined using data from the onboard GPS. An asterisk (*) in the Profile or Transect column indicates a time when a Terra (MISR) overpass occurred. Mean [with one standard deviation (SD)] and maximum RH values for each profile and transect are presented, as well.

Profiles:

Date (2001)	Profile	Range of horizontal position in aircraft profile (km) Zonal	Meridional	Altitude range (km MSL)	Relative humidity (%) Mean ± 1 SD	Max	Duration (min)
17 Jul	1	10.7	8.9	0.10–3.63	60 ± 12	79	32
	2	6.2	4.4	1.91–2.98	63 ± 10	78	4
	3	18.7	8.9	1.01–2.08	58 ± 7	66	4
	4	24.9	2.2	0.31–1.19	46 ± 10	65	5
	5	4.5	4.4	0.21–1.59	57 ± 4	64	5
	6	19.6	17.7	0.68–1.56	61 ± 9	76	5
	7	7.2	8.9	0.70–1.15	58 ± 7	71	2
	8	15.8	23.2	0.11–1.10	54 ± 8	64	7
2 Aug	1	8.0	16.6	0.05–1.83	66 ± 3	72	5
	2	23.1	14.4	0.05–3.18	57 ± 19	76	30
	3	24.9	13.3	1.00–3.17	50 ± 20	74	10

Transects:

Transect	Range of horizontal position in aircraft transect (km) Zonal	Meridional	Altitude (km MSL)	Relative humidity (%) Mean ± 1 SD	Max	Duration (min)
A	16.8	102.9	0.66	40 ± 3	49	14
B	65.0	26.5	2.92	71 ± 7	83	25
C	73.9	15.5	2.99	75 ± 4	86	20
D	27.6	14.4	2.06	60 ± 5	73	12
E	44.5	6.6	2.15	74 ± 4	84	15
F	52.5	16.6	0.97	36 ± 4	45	13
G	50.8	5.5	1.13	45 ± 5	56	14
H*	73.0	7.7	0.04	72 ± 4	84	16
I	11.6	7.7	0.20	63 ± 4	73	29
J	57.6	101.8	1.12	62 ± 6	83	21
A	28.4	90.7	1.88	58 ± 7	78	22
B*	44.5	1.1	0.07	70 ± 3	77	9
C	45.4	2.2	0.03	71 ± 3	80	9
D	53.4	0.0	0.94	69 ± 5	80	11
E	24.8	108.4	0.93	62 ± 12	83	26
F	111.6	84.1	0.52	62 ± 7	80	40

made from the FAA control tower at Paine Field, Washington State. All three instruments were calibrated during CLAMS (on 14 July 2001) with the Wallops Island National Weather Service (NWS) rawinsonde. No correction was applied to the raw Rosemount pressure measurements. The following correction to the raw temperatures (T_{raw}) was needed:

$$T_{\text{corrected}} = 0.98 T_{\text{raw}} + 0.9. \qquad (1)$$

In postanalysis, dewpoint temperatures needed to be raised by 0.5°C.

b. Optical parameters

Magi et al. (2005) describe the use of the custom-built MS Electron integrating three-wavelength (450, 550, and 700 nm with a nominal 40-nm bandwidth) nephelometer aboard the Convair-580 during CLAMS to measure dry aerosol light scattering coefficient, σ_{spd}. The MS Electron integrating nephelometer is similar to the commercially available TSI nephelometer (Anderson et al. 1996; Anderson and Ogren 1998), but it had an improved (closer to Lambertian) light source. Hartley et al. (2000) discuss the corrections for forward angular truncation and non-Lambertian illumination to give the total aerosol scattering coefficient (0° to 180°) and the hemispheric backscattering coefficient (90° to 180°). The authors also discuss the accuracy of the light scattering coefficient measurements (~10%). The nephelometer was calibrated on 17 April 2001 (prior to) and on 15 October 2001 (after) CLAMS, following the procedure given by Anderson et al. (1996).

The airstream to the nephelometer was heated to dry the aerosol and lower the RH to ~30%, thereby eliminating the effects of ambient RH on the measured aerosol light scattering and backscattering coefficients. To allow for the effects on the ambient scattering coefficients of ambient RH varying during CLAMS from 40%–80%, with a mean of ~60%, a humidification correction factor, $f(\text{RH})$, was applied to the dry aerosol light scattering coefficient measurements, adjusting them to the ambient RH. For this purpose, we used the empirical expression for hygroscopic growth derived by Kotchenruther et al. (1999), from data collected during the Tropospheric Aerosol Radiative Forcing Observational Experiment (TARFOX), a field campaign conducted in 1996 in the same region and time of year as CLAMS (Hobbs 1999):

$$\sigma_{\text{sp}} = \sigma_{\text{spd}}[1 + a(\text{RH}/100)^b], \qquad (2)$$

where a and b are fitting parameters that vary with air parcel back trajectories. Use of Eq. (2) assumes that the aerosol in CLAMS was of similar size and composition

to aerosol measured by Kotchenruther et al. (1999). As will be discussed later, values of ω_0 and various size parameters were virtually identical in the two campaigns, but the aerosol composition differed as discussed by Magi et al. (2005), who explain that we can assume the Kotchenruther et al. (1999) results provide a lower bound for the RH growth for CLAMS and use the theoretical growth curve parameterizations for pure sulfate aerosols as determined by Li et al. (2001) to estimate an upper bound. Since Magi et al. (2005) show that aerosol composition during CLAMS was dominated by sulfate, we can determine the degree of acidity of the pure sulfate aerosol based on a study by Brook et al. (1997) and air parcel back trajectories during CLAMS. Using these upper and lower limits for $f(\text{RH})$, we found that the uncertainty associated with using Eq. (2) to ultimately calculate values of ω_0 was ≤4%. Also, it should be noted that Eq. (2) does not work well to describe hygroscopic growth at low RH (i.e., <40%). Regarding Convair-580 flight paths on the two days of interest, the RH was <40% only at altitudes >2.5 km on 2 August 2001. For these measurements, we have assumed a hygroscopic growth factor of 1.0.

Figure 2 shows air parcel back trajectories at various altitudes for the 17 July and 2 August flights, which were obtained using the National Oceanic and Atmospheric Administration (NOAA) HYSPLIT analysis tool (available online at www.arl.noaa.gov/ready/hysplit4.html). Kotchenruther et al. (1999) considered three broad back trajectory classifications: westerly, northerly, and southerly flows. During CLAMS, a few days had back trajectories with an easterly near-surface component. In these cases, fit parameters for northerly or southerly flows were used since they were less influenced by anthropogenic sources than westerly flows. Values of these fitting parameters (along with ω_0 values at a wavelength of 550 nm) are listed in Table 3.

Magi et al. (2005) discuss the use of the Radiance Research custom-built Particle and Soot Absorption Photometer (PSAP) to measure dry aerosol light absorption coefficient, σ_{apd}, at a wavelength of 567 nm (15-nm bandwidth) aboard the Convair-580 during CLAMS.

Bond et al. (1999) and Bodhaine (1995) discuss corrections we employed for errors in sample spot size, instrument-to-instrument variability, instrument noise, and PSAP response to scattering and absorption. Magi et al. (2005) further elaborate on these corrections and others to the PSAP measurements ensuring coincident timing with the nephelometer, as well as appropriate adjustments to ambient temperature and pressure. The PSAP was calibrated on 17 April 2001 prior to the CLAMS campaign, as well on 15 October 2001 after the
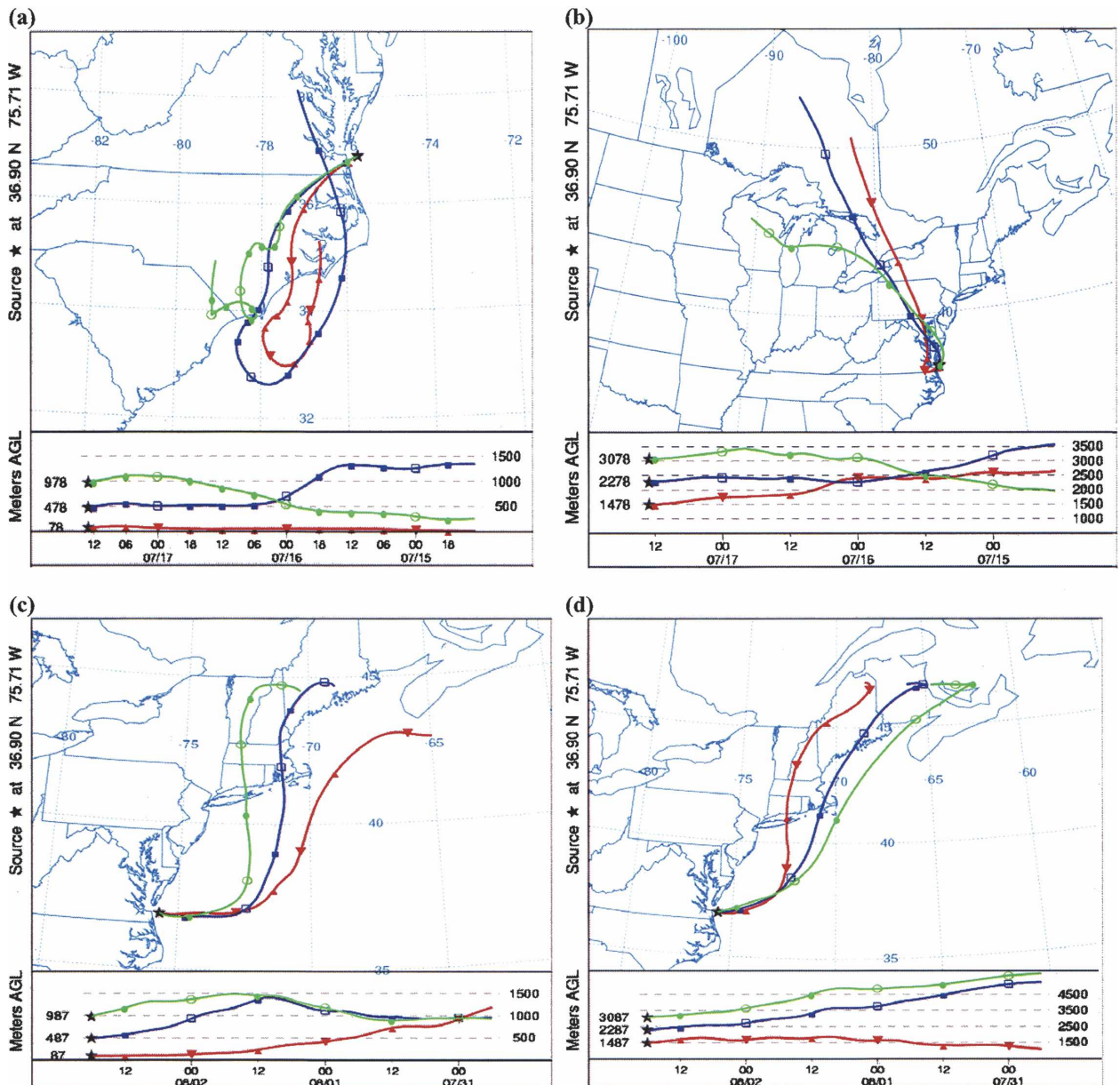
FIG. 2. Air parcel 72-h back trajectories at (a) 100 m (red triangles), 500 m (blue squares), and 1000 m (green circles) MSL, and (b) 1500 m (red triangles), 2300 m (blue squares), and 3100 m (green circles) MSL for 17 Jul 2001 over the East Coast determined with NOAA's HYSPLIT analysis tool. Note the circulation of the air near the surface over the coastal Atlantic states in (a), and how the air aloft in (b) comes from the north-northwest and was therefore influenced by emissions from southern Ontario and the mid-Atlantic states. (c), (d) The 72-h back trajectories at the same altitudes for 2 Aug 2001. The star off the coast of Virginia marks the location of the Chesapeake Bay Lighthouse. Altitudes of airflow back trajectories are listed at the bottom of each panel.

campaign, by comparing PSAP measurements of absorption coefficient to the difference between independently measured values of light scattering coefficient from light extinction coefficient values, as described by Bond et al. (1999). The accuracy of the PSAP measurements is ~25%, with larger percentage errors at lower values of light absorption.

The AOD values discussed in this paper were derived from measurements made by the AATS-14 aboard the Convair-580 aircraft. Redemann et al. (2005) discuss the operating principles and methods for data reduction, calibration, and error analysis applied to AOD data derived from the AATS-14 in CLAMS. In brief, the AATS-14 measures direct solar beam

TABLE 3. Fitting parameters a and b [derived from Kotchenruther et al. (1999)] used to correct dry light scattering coefficient values to account for hygroscopic growth; see Eq. (2). Single-scattering albedo (ω_0) values at a wavelength of 550 nm for all transects and profiles for the two Convair-580 flights of interest.

Date (2001)	Profile	Convair-580-derived ω_0 (mean ω_0 for entire profile)	Transect	Convair-580-derived ω_0 (mean ω_0 for entire transect)	Airflow back trajectory	
					Northerly/southerly $a = 1.71 \pm 0.04$ $b = 3.41 \pm 0.16$	Westerly $a = 3.20 \pm 0.02$ $b = 3.78 \pm 0.04$
17 Jul	1	0.97 ± 0.01	A	0.95 ± 0.01	Transects:	Transects:
	2	0.95 ± 0.04	B	0.98 ± 0.01	B, C, D, E	A, F, G, H, I, J
	3	0.97 ± 0.02	C	0.99 ± 0.01	Profiles:	Profiles:
	4	0.95 ± 0.03	D	0.94 ± 0.02	1 (1.5–3.6 km), 2,	1 (0.1–1.5 km),
	5	0.97 ± 0.01	E	0.97 ± 0.01	3 (1.5–2.1 km)	3 (1.0–1.5 km),
	6	0.97 ± 0.01	F	0.93 ± 0.03		4, 5, 6, 7, 8
	7	0.94 ± 0.01	G	0.94 ± 0.01		
	8	$0.96 \pm {<}0.01$	H	0.98 ± 0.01		
			I	0.97 ± 0.01		
			J	0.97 ± 0.01		
2 Aug	1	0.88 ± 0.02	A	0.91 ± 0.03	Transects:	Transects:
	2	0.93 ± 0.03	B	0.88 ± 0.02	A, B, C, D, E, F	N/A
	3	0.89 ± 0.03	C	0.89 ± 0.02	Profiles:	Profiles:
			D	0.94 ± 0.01	1, 2, 3	N/A
			E	0.93 ± 0.01		
			F	0.92 ± 0.04		

transmission in narrow spectral channels using sensors in a tracking head that can rotate about two axes. The instrument's tracking head mounts external to the aircraft skin to minimize blockage by aircraft structures and also to avoid data contamination by aircraft-window effects.

Since sunphotometers have a nonzero field of view, they measure some diffuse light in addition to the direct solar beam. As a result, uncorrected sunphotometer measurements can overestimate direct-beam transmission and thus, wavelength-dependent AOD values. This effect is amplified as wavelength decreases and as particle size increases in the column. However, since very small particles dominated size distributions in CLAMS, Redemann et al. (2005) state that these diffuse light corrections were generally negligible. The AATS-14 was calibrated in June 2001 prior to, and in September 2001, after CLAMS, at the Mauna Loa Observatory, Hawaii, using the Langley plot technique (Schmid and Wehrli 1995).

c. Particle size distributions

Particle size distributions were measured with a Particle Measuring Systems (PMS) Passive Cavity Aerosol Spectrometer Probe (PCASP) and a PMS Forward Scattering Spectrometer Probe (FSSP-300), both mounted under the wing of the Convair-580, as well as with a TSI Model 3320 Aerodynamic Particle Sizer (APS) located inside the aircraft (Willeke and Baron

1993). Total particle number concentrations were measured with a TSI Model 3022A condensation particle counter (CPC) and a TSI Model 3025A ultrafine condensation particle counter (Alam et al. 2003), both located inside the aircraft.

Hartley et al. (2000) discuss the operating principles behind the PCASP. A calibration of the PCASP prior to CLAMS on 19 April 2001 was performed using non-absorbing polystyrene spheres of varying diameter (2.020, 1.530, 0.804, 0.343, 0.198, and 0.142 μm). However, the diameter limits of the bins had to be adjusted to account for the difference between the expected aerosol refractive index and that of the calibrating polystyrene spheres (Liu et al. 1992). As Hartley et al. (2000) discuss, the channel diameter limits were corrected assuming an aerosol with a refractive index of $n = 1.46$–$0.0086i$. As a result, the PCASP classified particles into one of fifteen size channels with diameters ranging from 0.11 to 4.52 μm. A mid-CLAMS calibration was performed on 21 July 2001 using polystyrene spheres of the same size as in the 19 April calibration. Results were sufficiently similar to retain the channel limit corrections already in place.

The FSSP-300 is an optical particle counter, although it operates differently from the PCASP; a detailed description is given by Baumgardner et al. (1992). Measurements by the FSSP-300 are affected by Mie scattering, uncertainties in the index of refraction of the aerosol, nonuniform laser intensity, uncertainties in sample

volume, and time response roll-off. After applying corrections for these uncertainties, as discussed by Baumgardner et al. (1992) and Kim and Boatman (1990), the uncertainties in the particle number concentrations reported here were determined to be ~25%.

The FSSP-300 was calibrated prior to CLAMS on 2 May 2001. Nonabsorbing glass spheres (with diameters of 8.1, 15.7, and 21.9 μm) and polystyrene spheres (with diameters of 0.343 and 0.705 μm) were used in this calibration. The diameter limits of the channels were corrected to account for the differences in index of refraction between the encountered aerosol and that of the calibrating spheres. Using a mean RH in CLAMS of ~60%, Table 1 in Kim and Boatman (1990) was used to determine the average index of refraction of the aerosol we sampled ($n \approx 1.47$–$0.034i$). Since the air sampled during CLAMS had both urban and marine properties, this mean value was obtained by averaging the refractive indices these authors employed for urban and maritime aerosol models, respectively. This index of refraction ($n \approx 1.47$–$0.034i$) was then used to determine the channel size limits using Table 2 in Baumgardner et al. (1992). Although an estimation of the aerosol refractive index via this method is not ideal, it is the best we could attain given the measurements analyzed here. As a result, the FSSP-300 classified particles into one of 31 size channels with diameters ranging from 0.35 to 20.72 μm, though aerosols with diameters greater than ~5 μm were not encountered during CLAMS. A mid-CLAMS calibration was performed on 21 July 2001 using glass spheres 15.7 μm in diameter and polystyrene spheres with diameters of 0.705 and 0.343 μm. The results obtained were such as to retain the channel limit corrections already in place.

The TSI 3320 APS is a "time of flight" aerosol particle size spectrometer described by Wang et al. (2002). It measures the aerodynamic diameter of particles based on timing particle velocity between two laser beams, whereas the PCASP and FSSP-300 classified particles according to their optical diameters. As a result, the following correction was applied to the bin limits of the TSI 3320 APS (Murphy et al. 2004):

$$D_{\text{optical}} = D_{\text{aero}}/(\rho)^{0.5}, \tag{3}$$

where D_{optical} is the optical diameter, D_{aero} the aerodynamic diameter, and ρ the mean particle density, which we assumed to be 1.9 g cm^{-3} based on compositional data showing a strong dominance of sulfate (Castanho et al. 2005). With this correction, the TSI 3320 APS classified particles into one of 52 channels with diameter limits ranging from 0.36 to 14.4 μm. Unlike the PCASP and FSSP-300, which were mounted under the

wing of the Convair-580 aircraft, the TSI 3320 APS was located inside the aircraft, which limited the TSI 3320 APS diameter range to <1.0 μm. Stein et al. (2002) discuss how the TSI 3320 APS is subject to problems such as counting "phantom" particles and recirculation, which may lead to some particles being counted more than once. However, the authors state that these erroneous measurements affect measurements of particles with $D_p > 1.0$ μm, and therefore no additional correction has been applied to our TSI 3320 APS data. Since the APS was purchased only about a year prior to CLAMS, and was in relatively good agreement with the PCASP and the FSSP-300 measurements, it was assumed that the data output from the TSI 3320 APS could be used in qualitative assessments of particle size distributions and total particle number concentrations.

The TSI 3022A and TSI 3025A CPCs were located inside the Convair-580 aircraft during CLAMS. The TSI 3022A can detect particles with diameters ≥0.007 μm and is capable of measuring concentrations up to 10^7 cm^{-3}. The TSI 3025A can detect particles as small as 0.003 μm in diameter in concentrations of up to 10^5 cm^{-3}. However, because of their location inside the aircraft, these CPCs could not detect particles efficiently with $D_p > \sim 1.0$ μm. Alam et al. (2003) detail the operating principles of both CPCs.

d. Multiangle Imaging Spectroradiometer

MISR produces 36 simultaneous views of Earth, a combination of nine angles ranging from +70°, through nadir, to −70° in the along-track direction, in each of four spectral bands centered at 446, 558, 672, and 866 nm (Diner et al. 1998). It takes seven minutes for all nine MISR cameras to view a fixed, 400-km-wide line on the surface, which sets the swath width and effective temporal resolution for coincident observations. At midlatitudes, a given location is imaged about once per week in the MISR standard Global Imaging mode, providing 275 m spatial resolution data in all four nadir channels, and in the red channels, centered at 672 nm wavelength, of the other eight cameras. The remaining 24 channels of data are averaged on board the spacecraft to 1.1-km resolution.

The MISR aerosol retrieval algorithm compares observed, calibrated, multiangle radiances with those simulated for a range of particle mixtures and amounts. Column, spectral optical depth, and column effective aerosol mixture type are reported at 17.6-km resolution in the MISR standard aerosol product, which incorporates cloud screening and other considerations. Different algorithm approaches are used for overland and dark-water retrievals; overland, aerosol, and surface re-

flectance characteristics are retrieved self-consistently (Martonchik et al. 1998, 2002).

Prelaunch theoretical studies indicated that MISR spectral radiances, measured at precisely known air-mass factors ranging from 1 to 3, could provide tight constraints on aerosol column optical depths over land and water. [The airmass factor is the ratio of the slant path from the satellite through the atmosphere to the path along the nadir view, equal to $1/(\cos\phi)$, where ϕ is the zenith angle of observation.] Along with scattering angles ranging from about 60° to 160° at midlatitudes, MISR data provide constraints on particle shape, size distribution, and to a lesser degree, ω_0 values, particularly over dark, uniform ocean surfaces (Kahn et al. 1998, 2001). Generally, these studies predicted a column aerosol optical depth accuracy of at least 0.05 or 20%, whichever is larger. For good viewing conditions over ocean, this work predicted an ability to distinguish three-to-five size bins between about 0.1- and 2.5-μm diameter, two-to-four groupings of particle single-scattering albedo between about 0.8 and 1.0, and spherical particles from randomly oriented nonspherical particles, amounting to about a dozen categories of particle types. The predicted column optical depth sensitivity has been tested and verified globally (Kahn et al. 2005 and references therein), and has been analyzed in detail specifically for the CLAMS days discussed here (Redemann et al. 2005). Particle property retrieval validation is more challenging, since column-effective values of particle size distribution and single-scattering albedo values must be derived for comparison with the MISR results. The most reliable way of achieving this is to measure particle properties at multiple levels within the atmosphere and, to the degree possible, construct environmental snapshots of the entire column (e.g., Kahn et al. 2004). When utilizing such an approach with in situ aircraft data, the aerosol above the highest flight level must be accounted for in some way. Here, we determine the percent of AOD above the top flight level using AATS measurements to account for the aerosol aloft.

3. Results and discussion

a. General characterization of aerosol properties from the airborne in situ measurements

The data presented herein is a summary of the optical properties and size distributions of the aerosols measured from the Convair-580 aircraft on 17 July and 2 August 2001. Coincident MISR results are available for these two days.

1) STATE PARAMETERS

The hypsometric altitude of the aircraft allowed time/height cross-sections to be constructed for the 17 July and 2 August flights (Fig. 1). Similar flight patterns, consisting of multiple transects at altitudes ranging from ~0.05 to ~3.5 km MSL and vertical profiles covering the same altitude range, were conducted during the nine other flights of the Convair-580, allowing a fairly thorough characterization of atmospheric aerosol in the free troposphere. Temperature, RH, potential temperature, and latitudinal/longitudinal variability of measured parameters were derived from the measurements obtained in the vertical profiles and horizontal transects of both flights.

2) OPTICAL PROPERTIES

The aerosol single-scattering albedo is an important input to radiative forcing calculations. The single-scattering albedo was determined at a wavelength of 550 nm using

$$\omega_0 = \sigma_{sp}/(\sigma_{sp} + \sigma_{apd}). \qquad (4)$$

Figures 3a,b show measurements of the dry particle light absorption coefficient (σ_{apd}), the ambient particle light scattering coefficient (σ_{sp}) derived from Eq. (2), and ω_0 at 550 nm derived from Eq. (4), for the primary profiles of the 17 July and 2 August flights, respectively. The σ_{sp} profiles are similar to those measured at wavelengths of 450 and 700 nm (not shown), but σ_{apd} was measured only at 567 nm so we could not calculate ω_0 at these two wavelengths. Table 3 shows ω_0 values at 550 nm (with one standard deviation) for all transects and profiles of the 17 July and 2 August flights.

The dry aerosol light scattering coefficient measurements were corrected using Eq. (2) to account for hygroscopic growth of the aerosols in the ambient air. The values of a and b in Eq. (2) determined by Kotchenruther et al. (1999) were employed in our analysis using the air parcel back trajectories to identify probable aerosol type, as shown in Table 3. The light absorption coefficient measurements were not corrected for RH, since these are expected to be smaller than other uncertainties. Therefore, the measured dry values of absorption coefficient are used. The PSAP provided 30-s running means of σ_{apd} with outputs every second. Therefore, the nephelometer measurements of σ_{sp}, with outputs every second, were also averaged over 30 s. The effect of this averaging on spatial resolution is discussed in section 3b(1).

After applying the corrections discussed in section 2b, and when the air was quite clean, the values of scattering and/or absorption sometimes bordered on
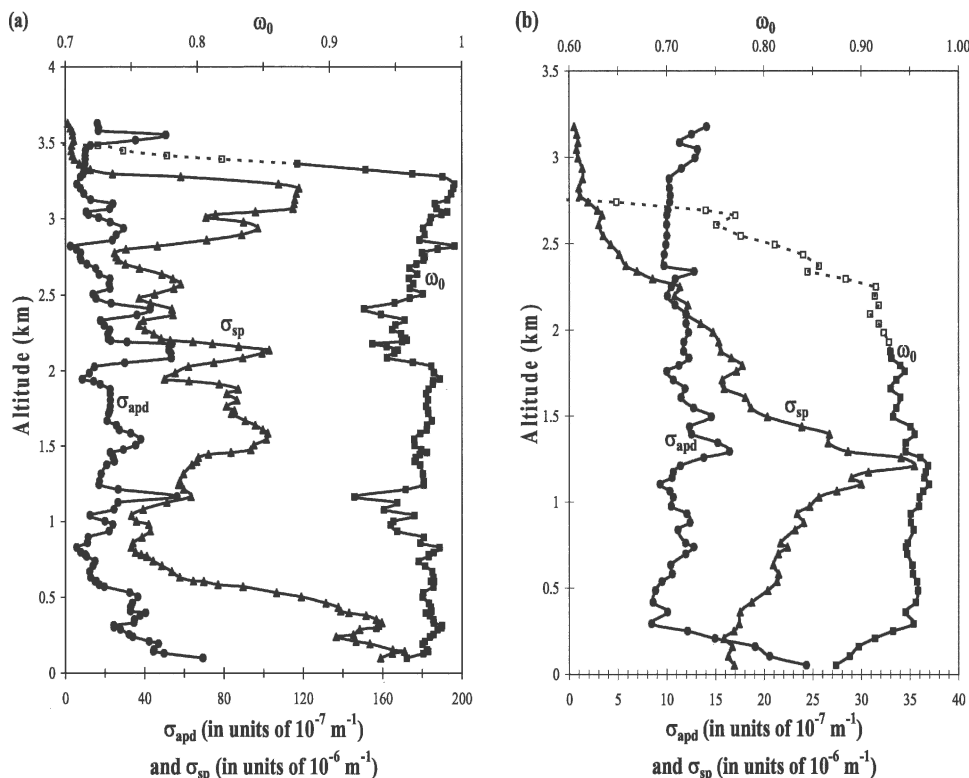
FIG. 3. Vertical profiles of σ_{apd} (circles), σ_{sp} (triangles), and ω_0 (squares) at a wavelength of 550 nm for (a) aircraft profile 1 of the 17 Jul 2001 flight, and (b) aircraft profile 2 of the 2 Aug 2001 flight. The dotted lines (with the open squares) in the single-scattering albedo (ω_0) profiles represent points where σ_{apd} is $\leq 3.0 \times 10^{-6}$ m^{-1} when σ_{sp} is $\leq 17.0 \times 10^{-6}$ m^{-1}. When this is the case, there is little aerosol present to be sampled. As a result, we lack confidence in these values of σ_{sp} and σ_{apd}, and thus in the derived ω_0 values, as well.

the detection limit of the instruments at altitudes >2–3 km. In these cases, the measured values of σ_{apd} were sometimes greater than the σ_{sp} values. Castanho et al. (2005) state that the black carbon (i.e., absorbing) content of the aerosol measured in CLAMS accounted for $3 \pm 1\%$ of those particles with $D_p < 2.5$ μm. Given the relatively low concentrations of absorbing aerosol, it is unlikely that σ_{apd} was, in reality, ever greater than σ_{sp}. In these layers aloft, particle number concentration was quite low as well (see Fig. 6). When the number concentration is low, we do not have confidence in the measured values of σ_{apd} and σ_{sp}; therefore, we ignore values of absorption less than 3.0×10^{-6} m^{-1} when scattering values are less than 17.0×10^{-6} m^{-1}, as Magi et al. (2005) have done before. These limits correspond to ω_0 of 0.85 at 550 nm. In Fig. 3, the sharp decrease in ω_0 at high altitudes is illustrated with dashed lines in profile 1 on 17 July and profile 2 on 2 August. We should point out that ω_0 values <0.85 may exist for aerosol above 2–3 km. However, the signals for σ_{sp}, σ_{apd}, and particle number concentration (Fig. 6) were quite low and/or began to decrease dramatically at

these altitudes; therefore, we do not have confidence in their accuracy and the derived ω_0 values.

It is noteworthy that some, but not all, profiles, including those shown in Fig. 3, show ω_0 decreasing with height, in particular at altitudes above 2–3 km MSL. This could be due to the typically decreasing RH with altitude and/or an increase in the relative amounts of carbonaceous to sulfate compounds with altitude, as suggested by Novakov et al. (1997). The values of ω_0 on 2 August are lower than on 17 July, indicating that the aerosol was more absorbing. This difference is supported by the results of Magi et al. (2005), who found there was a general trend of increasing carbon fraction with height for both 17 July and 2 August, as well as a higher total carbon fraction on 2 August. The latter result is interesting, since the total column AOD values at 525 nm were significantly lower on 2 August (0.09) than on 17 July (0.41). The absolute carbon and total mass concentrations on 17 July were 2–3 times greater than on 2 August (Magi et al. 2005). However, because of the higher fraction of absorbing aerosol on 2 August, we expect lower ω_0 values on that day. Differences in

aerosol properties may be expected based on air parcel history. Back trajectories show airflow at the surface from the south and from the northwest aloft on 17 July, whereas on 2 August, the airflow was easterly–northeasterly at the surface and aloft.

Figures 3a,b also capture the key features in CLAMS profiles not shown here. For example, haze layers are evident within about 0.3 km of the surface in the σ_{sp} profile of Fig. 3a, further aloft at ~3.1 km, and in Fig. 3b at ~1.2 km. In Fig. 3a, low aerosol loadings are present at ~1.0 km and ~2.8 km, where both σ_{apd} and σ_{sp} are relatively small. The sharp falloff in σ_{sp} (and RH) seen in some profiles at altitudes >0.5 km (e.g., Fig. 3a) marks the base of the free troposphere. Another interesting feature can be seen in Fig. 3b, where σ_{sp} diminishes by half between ~1.5 and 2.25 km, σ_{apd} changes by no more than 30%, but ω_0 changes little over this altitude range because it is already close to unity.

In comparing the mean ω_0 values at 550 nm for polluted layers (having $\sigma_{sp} > 30 \times 10^{-6}$ m^{-1}), we found that our CLAMS value of 0.96 ± 0.03 is very similar to the average ω_0 value of 0.95 ± 0.03 at 550 nm found by Hartley et al. (2000) during TARFOX. These results are summarized in Table 4.

3) PARTICLE NUMBER SIZE DISTRIBUTIONS

Particle number size distributions, $dN/d(\log D_p)$ where D_p is the aerosol diameter, dN the number concentration of aerosol with diameters $\geq D_p$ and $\leq D_p + dD_p$, are presented and discussed here for the flights on 17 July and 2 August. Plots (Figs. 4 and 5) represent time-averaged size distributions over the course of the individual transects comprising each layer.

To obtain the most representative total column particle size distribution from in situ aircraft data, we used a layer analysis. The vertical profiles flown in CLAMS do not produce reliable size distribution data from the PCASP or FSSP-300 measurements because of the pitch angle of the aircraft in these profiles affecting the flow of particles through these instruments. Consequently, we divided the 17 July and 2 August flights into layers represented by specific horizontal transects. For the 17 July flight we grouped transects to define four layers: (a) transects H and I for sea level to 0.5 km MSL; (b) transects A and F for 0.5–1.0 km MSL; (c) transects D, G, and J for 1.0–2.0 km MSL; and, (d) transects B, C, and E for 2.0–3.0 km MSL. Similarly, the 2 August flight was divided into the following four layers: (a) transects B and C for sea level to 0.5 km MSL; (b) transect F for 0.5–1.0 km MSL; (c) transects D and E for 1.0–1.5 km MSL; and, (d) transect A for 1.5–2.0 km MSL. This approach allows a useful comparison of

TABLE 4. Comparison of aerosol properties from the TARFOX and CLAMS field campaigns.

Parameter	TARFOX	CLAMS
ω_0 (550 nm, ambient RH)	0.94 (±0.03) (Hartley et al. 2000)	0.96 (±0.03)
Accumulation mode r_{eff}	0.12 μm (Tanre et al. 1999)	0.13 μm
Accumulation mode D_g	0.19 μm (Hartley and Hobbs 2001)	0.20 μm
Accumulation mode D_{smd}	0.24 μm (Russell et al. 1999)	0.24 μm
Accumulation mode D_{vmd}	0.27 μm (Smirnov et al. 2000)	0.28 μm
N (PCASP; 0.1 μm < D_p < 4.0 μm)	~1600 cm^{-3} (Hegg and Kaufman 1998)	800 ± 600 cm^{-3}
AOD (550 nm vs 525 nm)	0.30 ± 0.20 (Hegg et al. 1997)	0.13 ± 0.10

the in situ and MISR column-integrated particle size distributions, though it may introduce apparent horizontal spatial variability if grouped transects have different particle properties.

Table 5 lists particle size distribution results for the 17 July and 2 August flights for each layer, as well as for the total layer mean, which was derived by weighting the component layers by their respective AOD values. Table 6 lists particle size distribution results for each transect of both flights. Tables 5 and 6 also show the results from the surface area and volume distributions, though we do not discuss the results in detail here. As will be discussed in section 3b(3), comparison of the values in Table 5 with those in Table 6 reveals any large spatial variability introduced by averaging the various horizontal transects in a layer. However, there is little variability in the derived microphysical parameters, especially in the accumulation mode, when using this approach.

The size distribution of tropospheric aerosols is often characterized by four modes: the nucleation ($D_p < 0.01$ μm), the ultrafine (0.01 μm < D_p < 0.1 μm), the accumulation (0.1 μm < D_p < 1.0 μm), and the coarse particle ($D_p > 1.0$ μm), which can be used to describe a mix of airmass types, such as polar, maritime, continental, and urban (e.g., Jaenicke 1993; McMurry 2000). The accumulation and coarse particle modes are evident in the particle size distributions shown in Figs. 4 and 5. However, the instruments employed in this study were unable to measure size distributions for the nucleation and ultrafine modes.

Castanho et al. (2005) discuss the main sources of accumulation and coarse mode particles during CLAMS, based on filter measurements made aboard
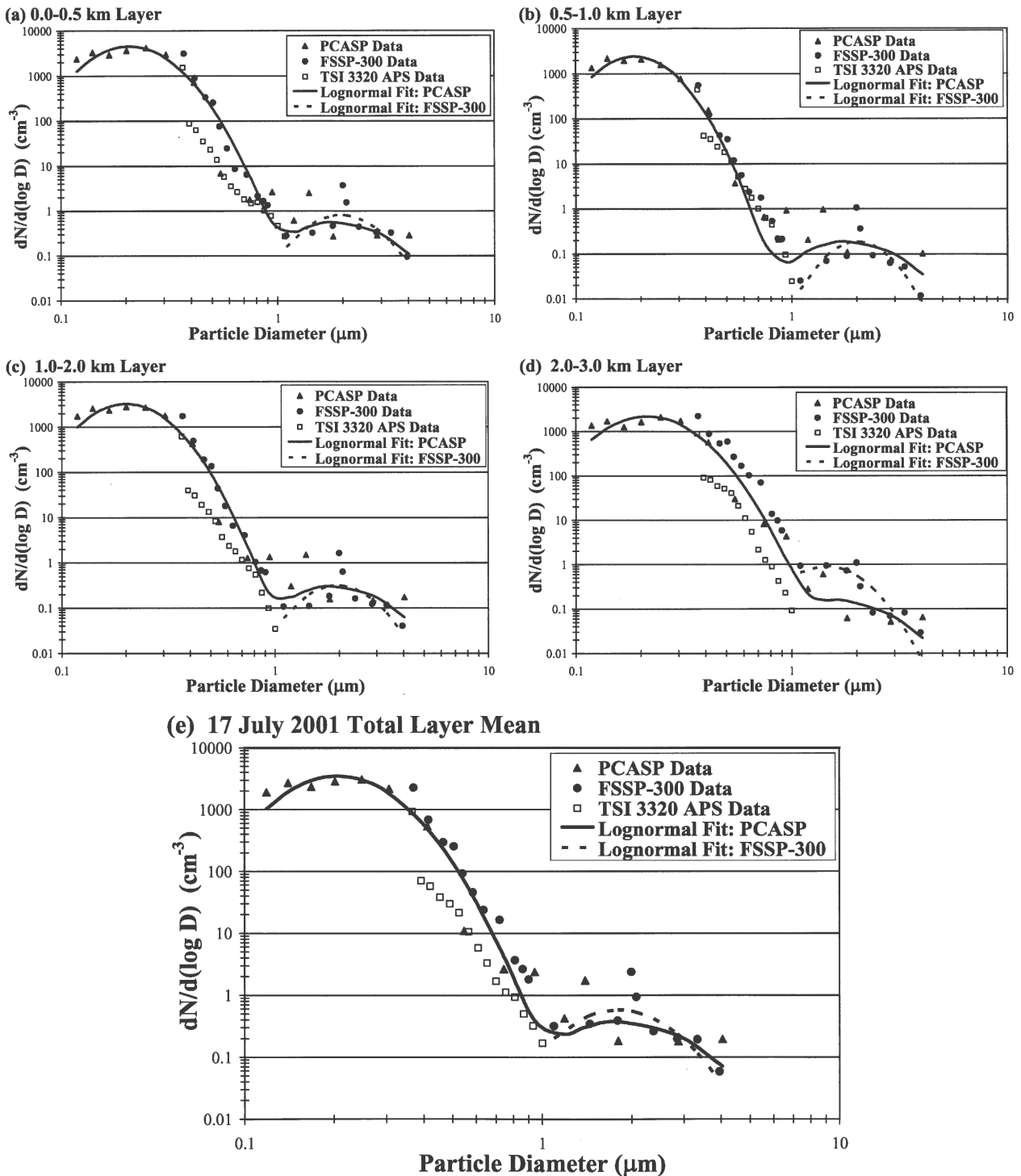
FIG. 4. (a)–(e) Particle number size distributions for the four layers, as well as the total layer mean, on the 17 Jul 2001 flight. Layers are defined in section 3a(3). Note the decreasing contribution of the accumulation mode with increasing altitude and the lognormally distributed accumulation mode with $D_g \approx 0.20$ μm in all layers. Table 5 shows values of D_g and associated values of σ_g for each layer. Table 6 lists particle size distributions for each component transect of the layers. Uncertainties associated with the measured particle number concentration from the three particle sizers are discussed in sections 2c and 3a(3).
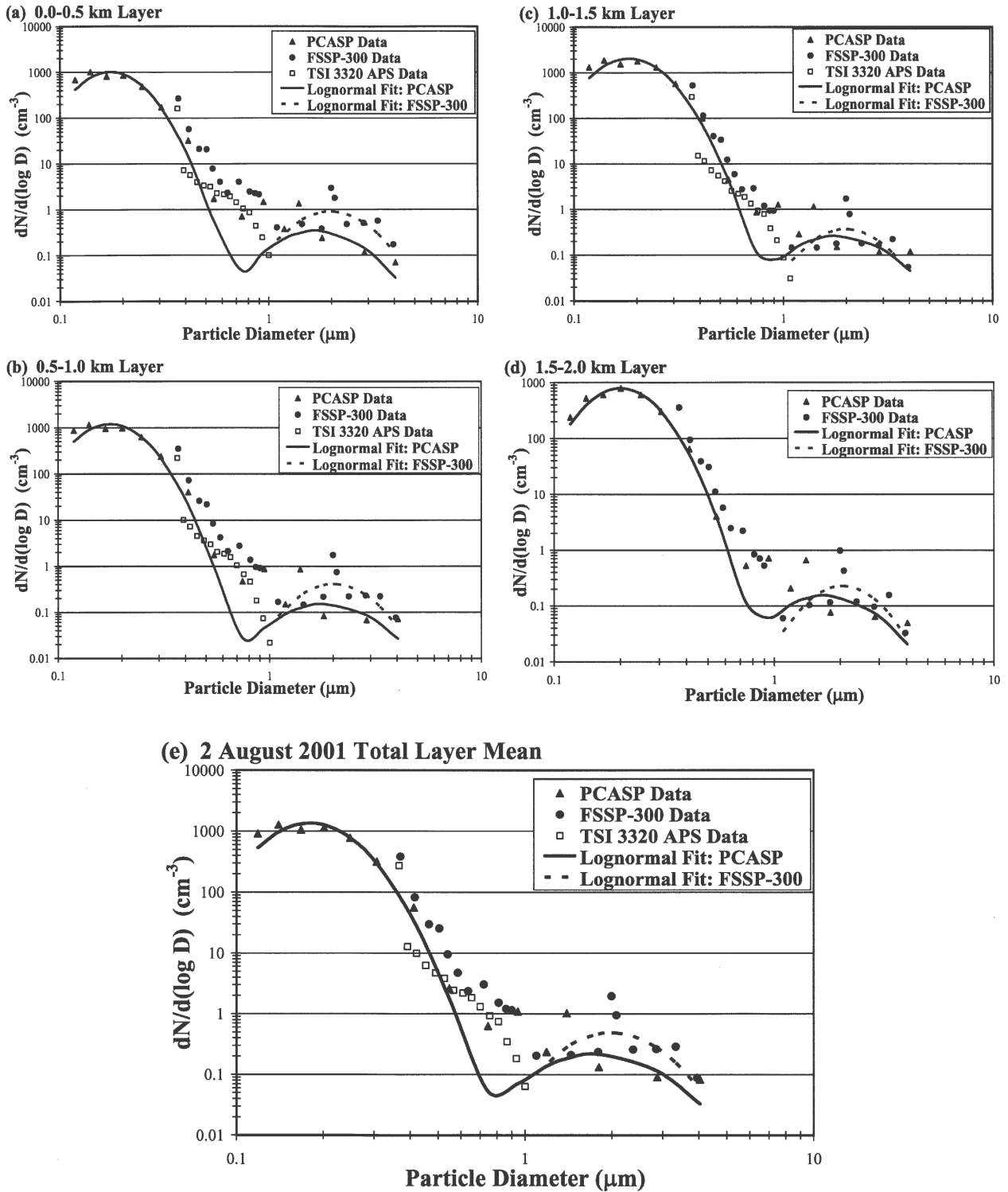
FIG. 5. As for Fig. 4, but for the 2 Aug 2001 flight. Note the lognormally distributed accumulation mode with $D_g \approx 0.20$ μm in all layers and the decreasing contribution of the coarse mode with increasing altitude. Uncertainties associated with the measured particle number concentration from the three particle sizers are discussed in sections 2c and 3a(3).

TABLE 5. Particle geometric median diameter (D_g), surface median diameter (D_{smd}), volume median diameter (D_{vmd}), geometric standard deviation (σ_g), effective particle radius (r_{eff}), and total particle number concentration (N) for the 17 Jul and 2 Aug flights. Values are presented as the averages of component transects within that layer, as discussed in section 3a(3). Accumulation mode D_g, D_{smd}, D_{vmd}, and σ_g values were derived using PCASP data, whereas coarse-mode values were derived with both PCASP and FSSP-300 data. The PCASP value is listed atop the FSSP-300 value for the coarse mode of each layer. Particle number concentration, as measured by the TSI 3025A particle counter, is listed (with one standard deviation) since the TSI 3025A can detect the smallest (and, therefore, majority of) particles. Some of the standard deviations associated with N are very large. This is because of the inhomogeneity in the sampled air as can be seen in Fig. 14.

Date (2001)	Layer (km MSL)	D_g (μm) Accumulation PCASP	D_g (μm) Coarse PCASP FSSP-300	D_{smd} (μm) Accumulation PCASP	D_{smd} (μm) Coarse PCASP FSSP-300	D_{vmd} (μm) Accumulation PCASP	D_{vmd} (μm) Coarse PCASP FSSP-300	σ_g Accumulation PCASP	σ_g Coarse PCASP FSSP-300	r_{eff} (μm) (MISR total column average r_{eff})	N (cm^{-3})
17 Jul	0.0–0.5	0.21	1.86 / 1.95	0.26	2.73 / 2.41	0.29	3.13 / 2.64	1.42	1.53 / 1.38	0.14	11310 ± 5079
	0.5–1.0	0.19	1.82 / 2.01	0.23	2.71 / 2.34	0.26	3.15 / 2.52	1.37	1.55 / 1.32	0.12	3529 ± 1709
	1.0–2.0	0.20	1.88 / 1.96	0.26	2.77 / 2.41	0.29	3.17 / 2.64	1.41	1.54 / 1.38	0.14	10767 ± 14465
	2.0–3.0	0.21	1.63 / 1.43	0.29	2.52 / 1.76	0.33	3.02 / 2.03	1.47	1.59 / 1.39	0.15	2333 ± 518
	Layer mean	0.21	1.84 / 1.80	0.26	2.73 / 2.29	0.29	3.13 / 2.55	1.42	1.54 / 1.41	0.14 [0.12]	6955 ± 8899
2 Aug	0.0–0.5	0.18	1.70 / 1.98	0.22	2.34 / 2.55	0.25	2.74 / 2.80	1.34	1.49 / 1.42	0.12	5375 ± 794
	0.5–1.0	0.18	1.83 / 2.00	0.22	2.67 / 2.53	0.25	3.08 / 2.78	1.35	1.53 / 1.40	0.12	2010 ± 259
	1.0–1.5	0.18	1.81 / 1.98	0.23	2.65 / 2.50	0.26	3.07 / 2.74	1.37	1.53 / 1.40	0.12	3221 ± 468
	1.5–2.0	0.20	1.71 / 2.05	0.25	2.50 / 2.54	0.28	2.93 / 2.77	1.36	1.54 / 1.38	0.13	1431 ± 423
	Layer mean	0.18	1.78 / 1.99	0.22	2.57 / 2.53	0.25	2.99 / 2.78	1.36	1.53 / 1.41	0.12 [0.12]	3006 ± 1551

TABLE 6. As in Table 5, but for each transect of the 17 Jul and 2 Aug 2001 flights.

Date (2001)	Transect	D_g (μm) Accumulation PCASP	D_g (μm) Coarse PCASP FSSP-300	D_{smd} (μm) Accumulation PCASP	D_{smd} (μm) Coarse PCASP FSSP-300	D_{vmd} (μm) Accumulation PCASP	D_{vmd} (μm) Coarse PCASP FSSP-300	σ_g Accumulation PCASP	σ_g Coarse PCASP FSSP-300	r_{eff} (μm)	N (cm^{-3})
17 Jul	A	0.19	1.82 / 2.03	0.24	2.66 / 2.32	0.27	3.08 / 2.47	1.38	1.53 / 1.29	0.13	4522 ± 1491
	B	0.22	1.61 / 1.41	0.30	2.52 / 1.71	0.34	3.04 / 1.97	1.48	1.59 / 1.38	0.16	2101 ± 255
	C	0.22	1.51 / 1.40	0.30	2.26 / 1.62	0.35	2.79 / 1.81	1.50	1.57 / 1.33	0.16	2042 ± 279
	D	0.20	1.86 / 1.90	0.25	2.81 / 2.49	0.28	3.21 / 2.78	1.40	1.55 / 1.44	0.13	2529 ± 694
	E	0.20	1.84 / 1.90	0.26	2.77 / 2.46	0.29	3.20 / 2.74	1.41	1.55 / 1.43	0.14	3129 ± 187
	F	0.19	1.82 / 1.99	0.23	2.74 / 2.36	0.26	3.19 / 2.56	1.37	1.56 / 1.34	0.12	2428 ± 1178
	G	0.19	1.82 / 2.03	0.23	2.72 / 2.46	0.26	3.15 / 2.67	1.37	1.55 / 1.36	0.12	3433 ± 889
	H	0.20	1.80 / 1.95	0.26	2.66 / 2.46	0.28	3.08 / 2.71	1.40	1.54 / 1.40	0.13	6824 ± 919
	I	0.21	1.89 / 1.96	0.27	2.77 / 2.37	0.30	3.15 / 2.59	1.43	1.53 / 1.36	0.14	13 723 ± 4750
	J	0.21	1.91 / 1.95	0.27	2.78 / 2.37	0.30	3.17 / 2.60	1.42	1.53 / 1.37	0.14	23 273 ± 24 143
2 Aug	A	0.20	1.71 / 2.05	0.25	2.50 / 2.54	0.28	2.93 / 2.77	1.36	1.54 / 1.38	0.13	1431 ± 423
	B	0.18	1.69 / 1.97	0.22	2.25 / 2.55	0.25	2.60 / 2.82	1.34	1.46 / 1.42	0.12	4981 ± 693
	C	0.17	1.71 / 1.98	0.21	2.42 / 2.54	0.25	2.85 / 2.79	1.34	1.52 / 1.41	0.11	5786 ± 675
	D	0.18	1.85 / 2.01	0.23	2.69 / 2.52	0.26	3.09 / 2.75	1.37	1.53 / 1.39	0.12	3534 ± 227
	E	0.18	1.79 / 1.97	0.23	2.63 / 2.49	0.26	3.05 / 2.74	1.36	1.54 / 1.40	0.12	3087 ± 480
	F	0.18	1.83 / 2.00	0.22	2.67 / 2.53	0.25	3.08 / 2.78	1.35	1.53 / 1.40	0.12	2010 ± 259

the Convair-580 and from surface sites. For the majority of flights, the main contribution to particle composition is from sulfate, although from 24–26 July, back trajectories indicate long-range transport of Saharan dust to our measurement site.

The particle number size distribution plots shown in Figs. 4 and 5 contain lognormal curves fitted to the PCASP and FSSP-300 data based on calculated values of D_g (the geometric median diameter) and σ_g, the geometric standard deviation (Reist 1993). For a lognormal distribution, a geometric standard deviation of 2 indicates that 67% of the values fall within a factor of 2 of the geometric mean. Several authors have discussed the applicability of a lognormal distribution to describe aerosol size distributions (e.g., Hoppel et al. 1994; Reid and Hobbs 1998). Since the use of lognormal curves to approximate aerosol distributions has been widely used, we will employ them here.

The curves in Figs. 4 and 5 representing the PCASP data are bimodal, indicating the presence of an accumulation mode and a coarse mode. For PCASP data, the accumulation mode covers a range of particle diameters from 0.11 to 1.00 μm, whereas the coarse mode covers particles with diameters from 1.00 to 4.52 μm. The FSSP-300 did not detect particles small enough to fully capture the accumulation mode. As a result, the lognormal curve was determined only for the coarse mode, defined as particle diameters ranging from 0.92 to 4.33 μm. Although the coarse mode bin limits for the PCASP and FSSP-300 are not exactly the same, they represent the closest particle diameter ranges given the bin limits of each instrument. The detection limits of the TSI 3320 APS prevented either the accumulation or coarse modes from being captured fully. In all cases, the lognormal particle number size distributions were determined using (Seinfeld and Pandis 1998; Makela et al. 2000):

$$dN_{\text{fit}}/d(\log D_p) = \{\Sigma[n_i/(2\pi)^{0.5} \log(\sigma_{g,i})]\} \exp\{-[\log(D_p)$$
$$- \log(D_{g,i})]^2/[2 \log^2(\sigma_{g,i})]\}, \qquad (5)$$

where the summation is taken for all bins in mode i, D_p is the particle diameter, and n_i the total number concentration in mode i. Table 5 lists the values of D_g, D_{smd} (the surface median diameter), D_{vmd} (the volume median diameter), and σ_g for both the accumulation and coarse modes for the previously defined layers of the 17 July and 2 August flights. Table 6 lists the same parameters, but for the individual transects of both flights.

The effective radius (r_{eff}) of the particle size distribution was calculated with accumulation mode PCASP data using (van de Hulst 1981):

$$r_{\text{eff}} = [\Sigma(r_p^3 n_i)]/[\Sigma(r_p^2 n_i)], \qquad (6)$$

where the summation is taken over all bins in the mode i, and r_p is the particle radius. Values of effective radius using Convair-580 data are listed in Table 5 for the layers of the 17 July and 2 August flights, and Table 6 for all individual transects of both flights. Like the total layer mean values of D_g, D_{smd}, and D_{vmd}, the total layer mean r_{eff} values were calculated by weighting the component layers by their respective AOD values.

Figures 4a–e show particle number size distributions for the four layers, as well as the total layer mean, of the 17 July flight. The PCASP data, which has a lower detection limit than the FSSP-300 or TSI 3320 APS, shows a consistent accumulation mode at $D_g \approx 0.20 \ \mu$m. These peaks are probably due primarily to the growth of Aitken nuclei by coagulation into larger particles that have long residence times (Covert et al. 1996; Birmili et al. 2001).

There is fairly good agreement between all three instruments for $D_p \approx 0.4$–1.0 μm in the transects of both flights. For the coarse mode, the data from the three instruments are not in as good agreement as for the accumulation mode. There is a sudden drop-off in the TSI 3320 APS data, which is likely due to this instrument being located inside the aircraft, where the inlet tubes prevent particles with diameters much larger than $\sim$1.0 μm from entering the instrument. McMurry (2000) states that inlet losses during aircraft sampling of supermicron particles can be as high as 50%–90%, whereas Huebert et al. (1990) found that ambient values of submicron particles are underestimated because of inlet losses that may be as great as a factor of 2–10. Although we acknowledge losses may be this great for the TSI 3320 APS and the TSI 3022A and 3025A particle counters, all located inside the aircraft, a laminar flow device was employed in front of the PCASP and FSSP-300 which likely kept particle losses to the lower end of these ranges. The FSSP-300 results show a clear coarse mode at $\sim$2.0 μm in the lowest layers, whereas the coarse mode in the 2.0–3.0 km MSL layer (Fig. 4d) is at 1.4 μm. However, the PCASP coarse mode data do not fit a lognormal distribution as well as the FSSP-300 data, even though both instruments were mounted under the aircraft's wing and provided simultaneous measurements. Despite these differences, the coarse mode D_g derived from the lognormal fits agree quite well, showing a general trend of decreasing D_g with height and a total layer mean D_g value of $\sim$1.80 μm. There is not much variability in the magnitude of the particle number size distributions with height, indicating a well-mixed lower troposphere.

Figures 5a–e show particle number size distributions

TABLE 7. Nonlinear correlation coefficients, R^2, between accumulation and coarse-mode lognormal curves and PCASP, FSSP-300 results for the number size, surface area, and volume distributions. Values of $R^2 > \sim 0.75$ indicate that the lognormal curve does a good job in representing the results as determined from PCASP and FSSP-300 measurements.

Flight date	Layer	Accumulation mode (number size, surface area, volume distribution values)	Coarse mode (number size, surface area, volume distribution values)	
			PCASP	FSSP-300
17 Jul	0.0–0.5 km	0.862, 0.937, 0.941	0.089, 0.001, 0.352	0.354, 0.262, 0.215
	0.5–1.0 km	0.903, 0.972, 0.986	0.126, 0.010, 0.258	0.363, 0.259, 0.175
	1.0–2.0 km	0.894, 0.960, 0.963	0.073, 0.001, 0.331	0.340, 0.236, 0.171
	2.0–3.0 km	0.786, 0.919, 0.908	0.286, 0.287, 0.190	0.754, 0.465, 0.262
	Layer mean	0.861, 0.946, 0.947	0.119, 0.002, 0.315	0.333, 0.305, 0.237
2 Aug	0.0–0.5 km	0.889, 0.975, 0.927	0.308, 0.022, 0.101	0.349, 0.307, 0.391
	0.5–1.0 km	0.880, 0.960, 0.978	0.124, 0.020, 0.233	0.325, 0.239, 0.273
	1.0–1.5 km	0.880, 0.968. 0.988	0.140, 0.005, 0.293	0.324, 0.220, 0.215
	1.5–2.0 km	0.974, 0.993, 0.990	0.234, 0.050, 0.208	0.340, 0.217, 0.235
	Layer mean	0.892, 0.971, 0.986	0.197, 0.034, 0.211	0.339, 0.256, 0.308

for the four layers, as well as the total layer mean, for the 2 August flight. Similar to the number size distribution plots for the 17 July flight, a consistent accumulation mode is seen at $D_g \approx 0.20\ \mu$m. A sharp decline in the TSI 3320 APS data at $D_p \gtrsim 1.0\ \mu$m is seen in these figures, as was the case for 17 July. There are also displacements of the PCASP and FSSP-300 data beyond $D_p \approx 1.0\ \mu$m, possibly because of the assumptions made in estimating the index of refraction to correct the channel limits. Each of these figures shows a coarse mode with $D_g \approx 2.0\ \mu$m.

It should be noted that in Figs. 4 and 5 there is an interesting feature in the FSSP-300 coarse mode data; two data points lie above the coarse mode curve, with the left point above the right by roughly the same amount. A possible cause of this anomalous looking feature is the fact that the bin size limits we used from Table 2 of Baumgardner et al. (1992) actually list the same size limits for the three bins to the left and the three bins to the right of this distinct feature. In postanalysis, we have subdivided these bin ranges, hence there is very little variation in the magnitude of the three points to the left and right of this "spike" in the FSSP-300 coarse mode data. Furthermore, these coarse mode particles had extremely low number concentrations and, as will be discussed in section 3b(3), much of this data is likely to be instrument noise. Still, we find it of some use to present this data as well as the derived coarse mode size parameters as a means of describing the aerosol properties on these two days as fully as possible.

Unlike the particle number size distribution results from 17 July, there does not seem to be much variability with height in the value of coarse mode D_g for the 2 August data. However, Figs. 4a–d show a smaller con-

tribution from coarse mode particles to the particle number size distribution with increasing height on 17 July. We attribute this to large sea salt particles on the earlier date that settle out at low altitudes. This is supported by near-surface wind speed data measured aboard the Convair-580, as well as measurements made at the Chesapeake Lighthouse. The mean near-surface wind speed on 17 July was $5.5 \pm 2.1\ \mathrm{m\ s^{-1}}$ from the Convair-580 measurements, whereas mean surface winds of $8.2 \pm 2.2\ \mathrm{m\ s^{-1}}$ were measured at the lighthouse. Comparing these values to $3.7 \pm 1.2\ \mathrm{m\ s^{-1}}$ (Convair-580) and $4.4 \pm 1.1\ \mathrm{m\ s^{-1}}$ (Chesapeake Lighthouse) on 2 August, significantly stronger surface winds were present on 17 July, supporting our suggestion that more near-surface sea salt particles were present on 17 July. Also, in comparing the particle number size distributions from 2 August with those from 17 July, the aerosol loading on 2 August was significantly lower. The AATS results support this, yielding mean total column AOD values at 499 nm for 17 July and 2 August of 0.45 and 0.11, respectively (Redemann et al. 2005).

While we do not discuss the particle surface area and volume distributions here, values of D_{smd} and D_{vmd} are presented in Tables 5 and 6. Larger particles are weighted progressively more heavily in number size, surface area, and volume size distributions. However, the surface area and volume-weighted distributions on both 17 July and 2 August still show a dominance by accumulation mode particles.

Table 7 lists the correlation coefficients, R^2, for the nonlinear regressions between the lognormal curves and the PCASP, FSSP-300 results for the number size, surface area, and volume distributions on the 17 July and 2 August flights. If the R^2 value is greater than 0.75, we conclude that the lognormal curve does a good job
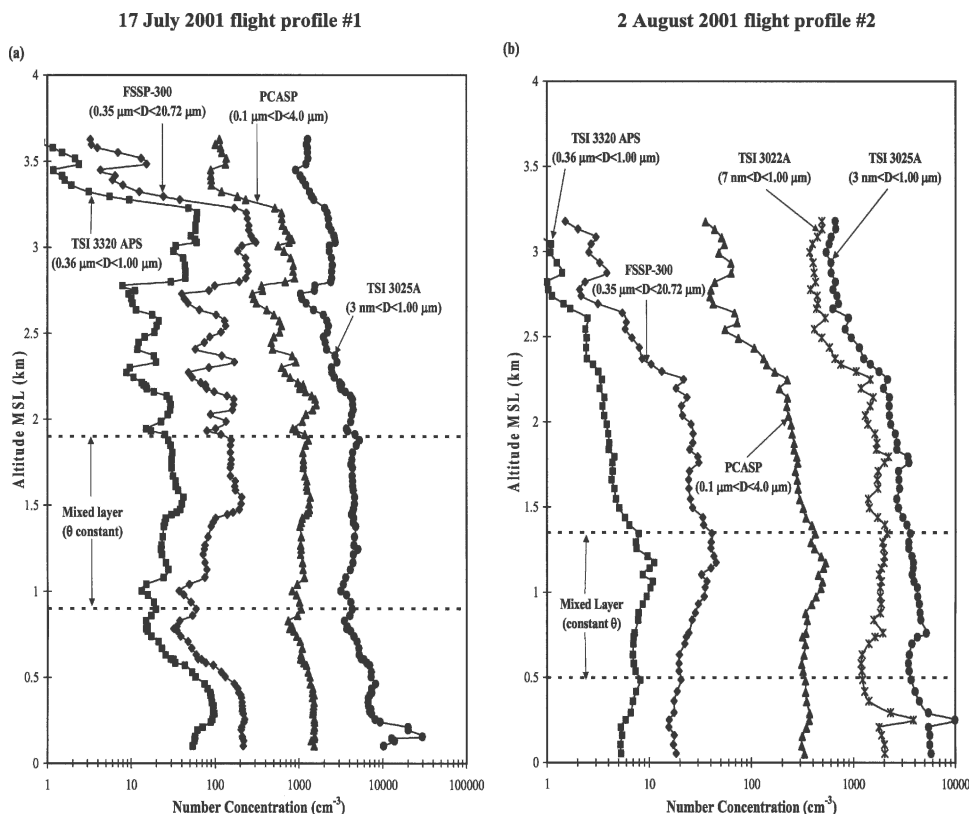
FIG. 6. Particle number concentrations measured by various particle counters for (a) profile 1 of the 17 Jul flight and (b) profile 2 of the 2 Aug flight. The dashed lines represent a mixed layer, where potential temperature (θ) was constant, associated with fairly constant particle number concentrations. Squares represent TSI 3320 APS, diamonds represent FSSP-300, triangles represent PCASP, asterisks represent TSI 3022A, and circles represent TSI 3025A. Uncertainties associated with these instruments are discussed in section 3a(3).

at representing the results from that particular optical particle sizer and, thus, the aerosol in that mode are lognormally distributed. The R^2 values in Table 7 indicate that the accumulation mode particles certainly appear to be lognormally distributed, whereas the coarse mode particles do not fit this distribution well.

In comparing the accumulation mode size parameters from CLAMS to those from TARFOX, we see that they are virtually identical. Tanre et al. (1999) report an accumulation mode r_{eff} of 0.12 μm for TARFOX, while the corresponding value for CLAMS was 0.13 μm. Hartley and Hobbs (2001) found that the mean accumulation mode D_g was 0.19 μm; in CLAMS accumulation mode D_g was 0.20 μm. Russell et al. (1999) calculated a mean accumulation mode D_{smd} of 0.24 μm; in CLAMS, the value was 0.24 μm, as well. Smirnov et al. (2000) determined accumulation mode D_{vmd} in TARFOX to be 0.27 μm; in CLAMS, the same parameter was 0.28 μm. These results are summarized in Table 4.

4) TOTAL NUMBER CONCENTRATION OF PARTICLES

The total number concentrations of particles (N) were measured for the main profile on 17 July (Fig. 6a) by the TSI 3320 APS over the size range: 0.5 μm < D_p < 1.00 μm, the FSSP-300 (0.35 μm < D_p < 20.72 μm), the PCASP (0.1 μm < D_p < 4.0 μm), and the TSI 3025A (3 nm < D_p < 1.00 μm). The TSI 3320 APS and TSI 3025A were located inside the Convair-580, which limited the maximum size particles that they could detect; the PCASP and FSSP-300 were located under the wing of the aircraft. During the 2 August flight, a fifth particle counter, the TSI 3022A (7 nm < D_p < 1.00 μm), was in operation for the flight's main profile (Fig. 6b). Uncertainties associated with the measurements made by these instruments are discussed in sections 2c and 3a(3). Typical mean total particle number concentrations measured during CLAMS were ~10^3 to 10^4 cm^{-3} when measured with the most sensitive particle

counter, the TSI 3025A. Since marine atmospheric particle concentrations are $\sim$100–300 cm^{-3}, there were some continental and/or anthropogenic contributions to the particles sampled. This is supported by the composition data presented by Magi et al. (2005).

Table 5 summarizes the total particle number concentrations, N, for the previously defined layers of the 17 July and 2 August flights, measured with the TSI 3025A particle counter. Table 6 lists N values for each horizontal transect of both flights. As a result of localized enhancements in N values at certain points in the transect, some of the listed values of N have associated standard deviations that are quite large relative to the mean value. Referring to Table 2, it can be seen on which transects large spatial areas were covered, and therefore nonhomogeneous air was likely sampled. Redemann et al. (2005) concluded that the AOD spatial variability during CLAMS was due to the transport and diffusion of similar aerosol types, rather than to mixing of aerosol types with different sizes and compositions.

July 17 was the more polluted of the two days, with a total mean layer particle number concentration of $\sim$7000 cm^{-3}, whereas the total layer mean particle number concentration on 2 August was $\sim$3000 cm^{-3}. At low levels on 17 July (Fig. 2a), the air recirculated over the coast for at least three days, allowing N to build up in the measurement region. Further aloft (Fig. 2b), the airflow was over the Great Lakes, and therefore carried continental and anthropogenically enhanced aerosols. In contrast, the airflow back trajectories on 2 August had a strong easterly/northeasterly (i.e., marine) influence at all levels up to $\sim$3 km (Figs. 2c,d), leading to the much lower particle number concentrations and AOD values on 2 August.

PCASP measurements of particle number concentrations during CLAMS were roughly half of those encountered during TARFOX, as shown in Table 4 (Hegg and Kaufman 1998). This was probably because of the different meteorological conditions during these two studies. Whereas measurements during CLAMS were generally obtained in relatively clean air that had recently passed over the Great Lakes or the Atlantic Ocean, airflows during TARFOX were more commonly from industrial and urban areas immediately to the west of the study area. As a result, the air sampled during TARFOX was more polluted than that during CLAMS. A well-defined mixed layer can be seen in the figure for the total particle number concentrations (as illustrated by dashed lines in Fig. 6). Measurements showed that these regions were characterized by potential temperature values that were steady with height, indicating that the air was well mixed and, as a result,

particle number concentrations were fairly constant with height.

b. Small-scale horizontal variability of aerosol properties

An analysis of the small-scale horizontal variability of aerosol properties is needed to determine: (a) whether an average radiance in a given scene, as measured by MISR, can readily be translated into an average aerosol parameter over the scene, and (b) whether the layer method employed in the particle size distributions is justified. Measured variability is the sum of ambient variations and measurement noise (Anderson et al. 2003). Therefore, as the authors explain, variability in aerosol properties can be studied only if instrument noise is known to be negligible or can be quantified and a correction applied. Here, we examine the lag-1 autocorrelation coefficient, $r(1)$, to evaluate instrument noise. For our analysis, we have chosen a time lag interval of 10 s, corresponding to a spatial resolution of $\sim$1 km, given the $\sim$100 m s^{-1} aircraft flight speed that was used throughout CLAMS. If the correlation $r(1)$ is $> \sim$0.99, the measurement is free of noise at the specified resolution and there is no significant ambient variability at this spatiotemporal scale. However, if $r(1) < \sim$0.97, the cause could be either instrumental noise or ambient variability.

Anderson et al. (2003) discuss the mesoscale variations of tropospheric aerosols and conclude that significant variability was present on time scales of <10 h and on spatial scales of $\sim$200 km or less. We are not concerned here with the temporal variability of the aerosol, since our flights lasted only 3–6 h. However, there may have been significant spatial variability, since we typically covered areas of hundreds of kilometers, both zonally and meridionally (Table 2). The vertical profiles were flown in tight spiral ascents and descents, virtually eliminating any horizontal inhomogeneities. Unlike the datasets discussed by Anderson et al. (2003), our flight strategy was not aimed at preferentially sampling aerosol plumes and gradients, but rather concentrated on flying simultaneous and coordinated flight paths with other platforms on which measurements were made.

1) OPTICAL PARAMETERS

Figure 7 shows the results from the autocorrelations for both σ_{sp} and σ_{apd} on 17 July and 2 August. On both days the r(1) value is $\geq \sim$0.99 for the σ_{sp} data, so we are confident there is no significant noise or variability in this parameter on spatial scales of $\sim$4 km. (The resolution is stated as $\sim$4 km since the PSAP and neph-
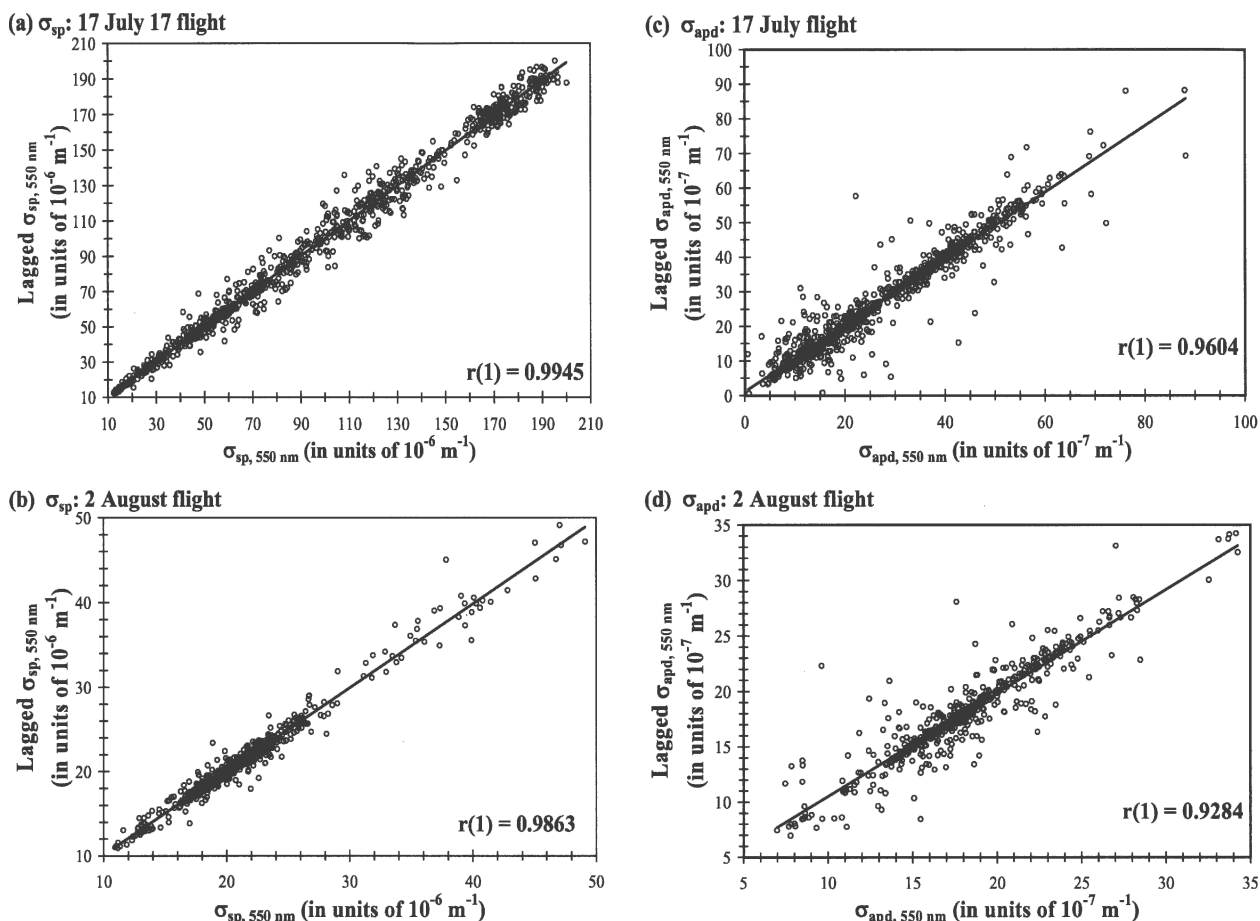
FIG. 7. Lag-1 autocorrelation for σ_{sp} [(a) 17 Jul and (b) 2 Aug] and σ_{apd} [(c) 17 Jul and (d) 2 Aug] measurements made with the nephelometer and PSAP, respectively. The lag is one measurement interval, which we have chosen to be 10-s or ~4-km resolution (due to 30-s running averages of PSAP and nephelometer data in addition to this 10-s averaging).

elometer data were processed with 30-s smoothing in order to reduce instrument noise. In addition, these 30-s running averages were averaged over 10-s intervals for the autocorrelation analysis, so the spatial resolution is ~4 km assuming an aircraft speed of ~100 m s^{-1}. The effect of this averaging on signal broadening is to reduce the magnitude of the most extreme maxima and minima in σ_{sp} and σ_{apd}. However, this effect is never >7% and results in a minimal adjustment in calculated ω_0 values of ~0.005.) However, the $r(1)$ values for σ_{apd} were 0.9604 on 17 July and 0.9284 on 2 August. Given the relative homogeneity in particle composition reported by Castanho et al. (2005) along with the very low σ_{apd} values throughout CLAMS, often bordering on the 1×10^{-7} m^{-1} detection limit of the PSAP, this poor correlation is likely a result of instrument noise rather than ambient variability in σ_{apd}.

Figure 8 illustrates the small-scale horizontal variability of σ_{apd}, σ_{sp}, and ω_0 at a wavelength of 550 nm for a few selected transects at various levels of the atmo-

sphere from both the 17 July and 2 August flights. These transects also illustrate ~4-km aerosol optical property variability in the other transects not presented here. One notable feature is the relatively uniform value of ω_0 throughout a given transect. (The standard deviation is ≤2% of the mean for all transects.) Although σ_{sp} and σ_{apd} vary, often σ_{sp} and σ_{apd} increase or decrease together, so ω_0 remains fairly constant. In some cases, a systematic increase in ω_0 can be seen because of a rise of σ_{sp} while σ_{apd} remained fairly constant (Fig. 8a). Conversely, Fig. 8c shows a gradual decrease in ω_0 associated with declining values of σ_{sp} and constant values of σ_{apd}. However, even in these two cases, the overall small-scale horizontal variability in ω_0 is minimal.

In transects where ω_0 shows some variability, the variability is mostly attributable to changes in σ_{apd} over the entire transect. It should be noted that the value of σ_{apd} throughout CLAMS was remarkably low (~10^{-7} m^{-1}) and as a result, ω_0 values are sensitive to small
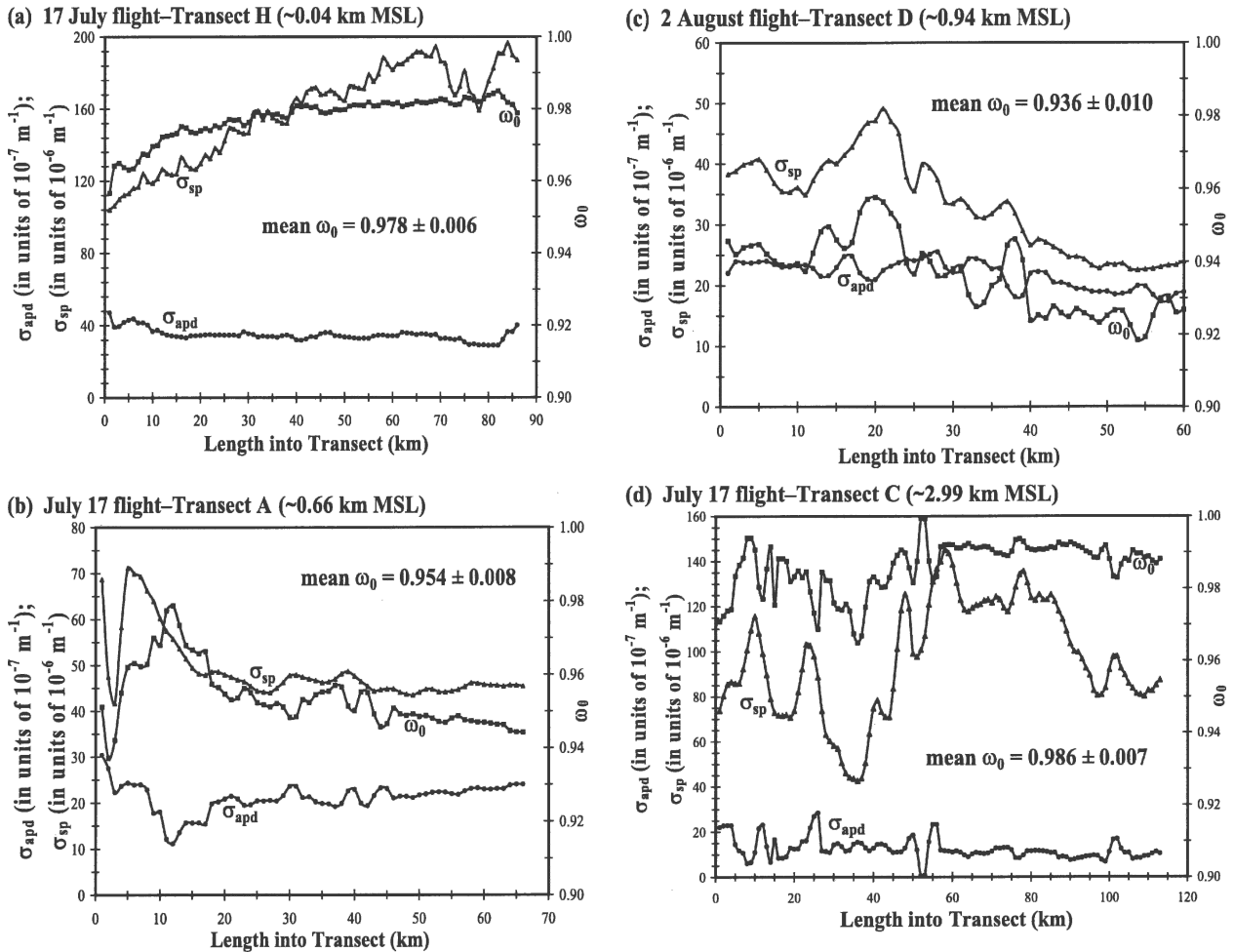
FIG. 8. Small-scale (~4 km) horizontal variability of σ_{apd}, σ_{sp}, and ω_0 at a wavelength of 550 nm for selected transects of the 17 Jul and 2 Aug flights.

changes in σ_{apd}. Also, unlike the sharp decline in ω_0 in the Fig. 3 profiles, the transects higher in the lower troposphere still show consistently high ω_0 values (e.g., Fig. 8d). However, none of the transects conducted on the two dates were at altitudes as high as the top of the profiles shown in Fig. 3, so this feature could not be analyzed further. We conclude that there is minimal variation in the value of ω_0 over horizontal scales of ~4 km and the optical parameters probably vary on scales of tens of kilometers or more.

2) AEROSOL OPTICAL DEPTH

The results presented here supplement the analysis carried out by Redemann et al. (2005). Figure 9 shows the results of the lag-1 autocorrelation for the AOD measurements on 17 July and 2 August. Redemann et al. (2005) discuss their AATS data reduction methods, calibration, and error analysis. Since the authors have already accounted for instrument noise in the AATS data provided to us, we do not discuss noise reduction here, and as expected, the $r(1)$ values are quite high—0.9987 for 17 July and 0.9965 for 2 August. We conclude that these data are free of noise at ~1-km resolution and that there is no significant ambient variability at this spatial scale.

Redemann et al. (2005) present results from their analysis of the small-scale horizontal variability in AATS-derived AOD throughout CLAMS. They also perform correlations between AATS-, Aerosol Robotic Network (AERONET)-, Moderate Resolution Imaging Spectroradiometer (MODIS)-, and MISR-derived AOD values. Their results show that AOD can vary by as much as 50%–70%, but more typically 25%–30% over horizontal distances of 50 km. Furthermore, they discovered that there was no spectral dependence of the relative variability in AOD. This suggests that the spatial variability in AOD during CLAMS was caused more by the transport and diffusion of similar aerosol

(a) 17 July flight

(b) 2 August flight
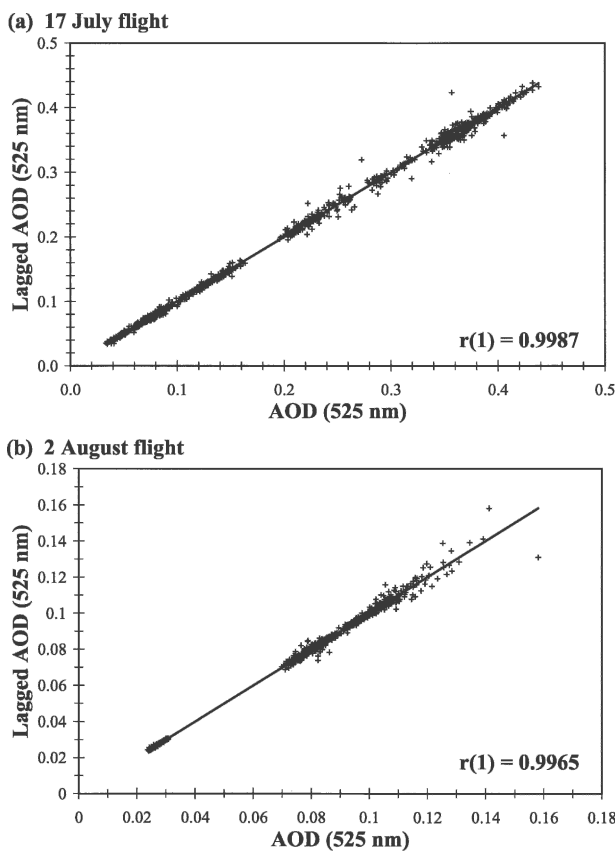
FIG. 9. Lag-1 autocorrelation for AOD measurements made with the AATS-14 on (a) 17 Jul 2001 and (b) 2 Aug 2001. The lag is one measurement interval, which we have chosen to be 10-s or ~1-km resolution.
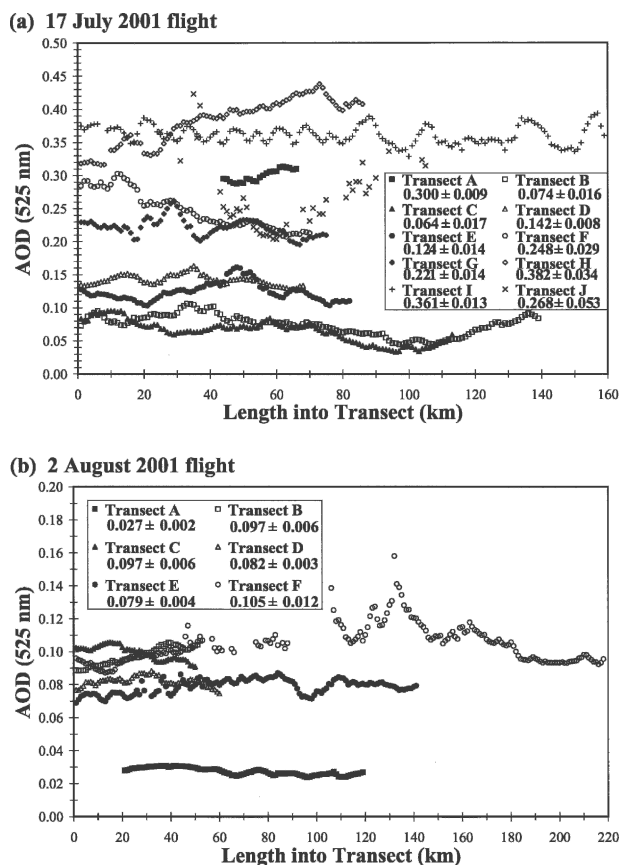
(a) 17 July 2001 flight

(b) 2 August 2001 flight

FIG. 10. Small-scale (~1 km) horizontal variability in AOD (at 525 nm) as measured by the AATS-14 for all transects of the (a) 17 Jul and (b) 2 Aug 2001 flights with means and one standard deviation reported below each transect label.

types rather than the mixing of aerosol types having different sizes and compositions. The transport and diffusion of similar aerosol types could create regions of higher or lower particle number concentration, which would likely create more or less light extinction in the region, and ultimately cause AOD spatial variability.

Figure 10 illustrates the horizontal variability in 525 nm AOD at ~1-km resolution for all transects of the 17 July and 2 August flights. The values presented in these figures were measured with the AATS-14 aboard the Convair-580 aircraft. As shown earlier in Fig. 9, these graphs demonstrate explicitly that AOD varies minimally even on horizontal scales of tens and sometimes hundreds of kilometers at all levels of the lower troposphere.

3) PARTICLE SIZE PARAMETERS

Figure 11 shows the results from the autocorrelations for fine- and coarse-mode particle number concentrations (N) as measured by both the PCASP and FSSP-

300 optical particle counters. On both days the $r(1)$ value is $\geq \sim 0.99$ for the fine-mode N data from the PCASP, so we are confident there is no noise or significant variability in this parameter at spatial scales of ~1 km. However, the $r(1)$ values for coarse mode N as measured by both the PCASP and FSSP-300 on both days (Figs. 11b,c,e,f) were quite low. Given that the vast majority of second-by-second number concentrations on both days were 0 cm^{-3} for all coarse-mode bins, we are unable to make any conclusions regarding the spatial variability of coarse-mode size parameters.

Figure 12 illustrates the small-scale horizontal variability of accumulation mode particle size parameters measured by the PCASP for a few representative transects of the 17 July and 2 August flights. Since D_{smd} is larger than D_g by a factor of $\exp[2\ln^2(\sigma_g)]$, and D_{vmd} is larger than D_g by a factor of $\exp[3\ln^2(\sigma_g)]$, any variability in D_g will be amplified in the determination of D_{smd} and D_{vmd}.

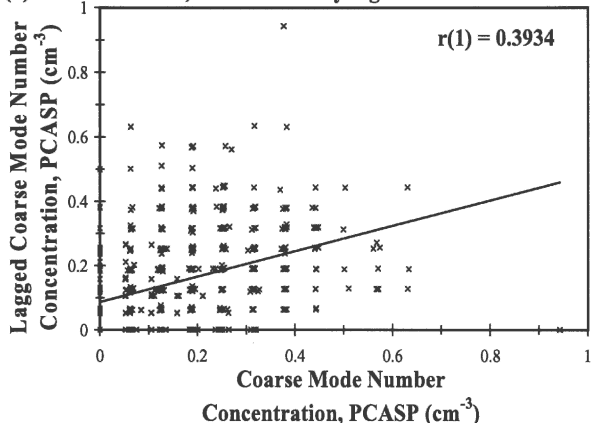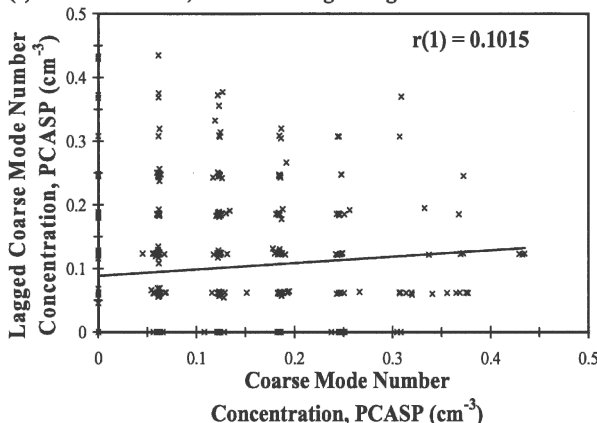Figure 12 shows extraordinarily little horizontal vari-
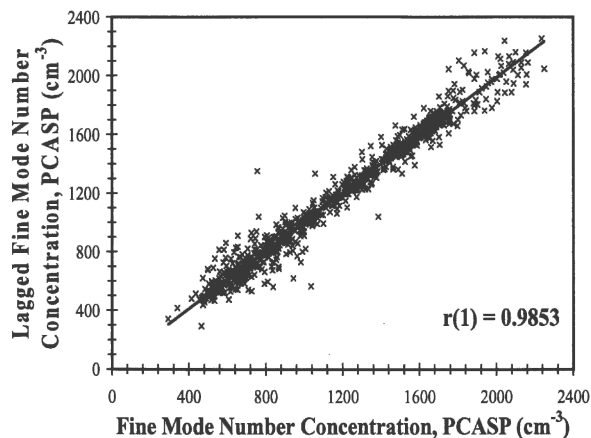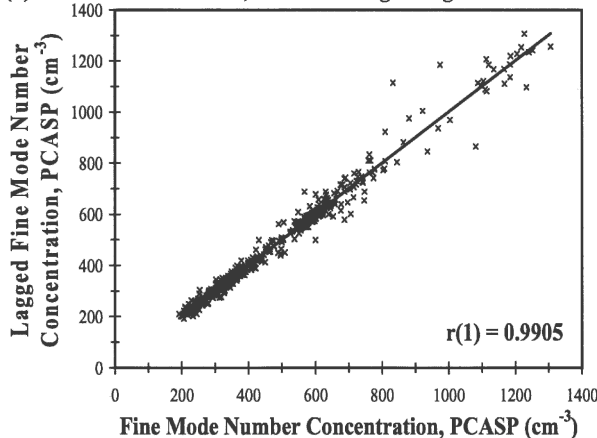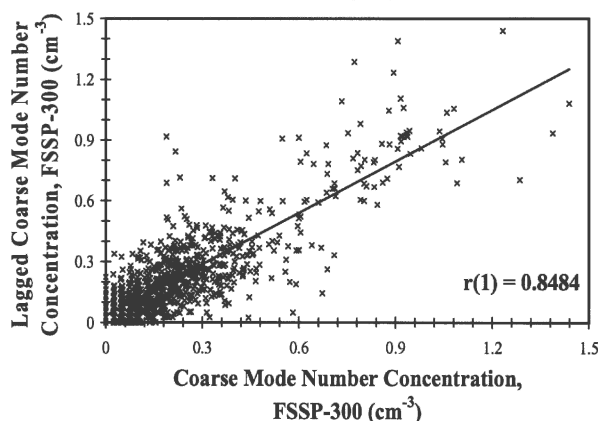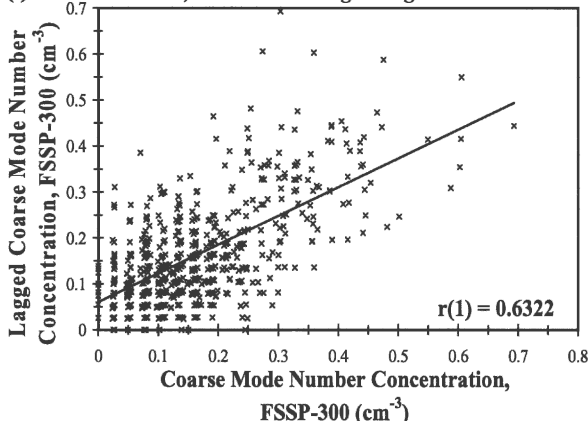
FIG. 11. Lag-1 autocorrelation for fine mode PCASP particle number concentration [(a) 17 Jul and (d) 2 Aug] measurements, coarse-mode PCASP particle number concentration [(b) 17 Jul and (e) 2 Aug] measurements and coarse mode FSSP-300 particle number concentration [(c) 17 Jul and (f) 2 Aug] measurements. The lag is one measurement interval, which we have chosen to be 10-s or ~1-km resolution.

ability in the accumulation mode size parameters at the lowest levels of the atmosphere, but slightly increasing horizontal variability with altitude. This could be attributable to increasing vertical variability as altitude in-

creases if the aerosol layers are not actually horizontal. Accumulation mode particles were systematically larger at all altitudes on 17 July than on 2 August.

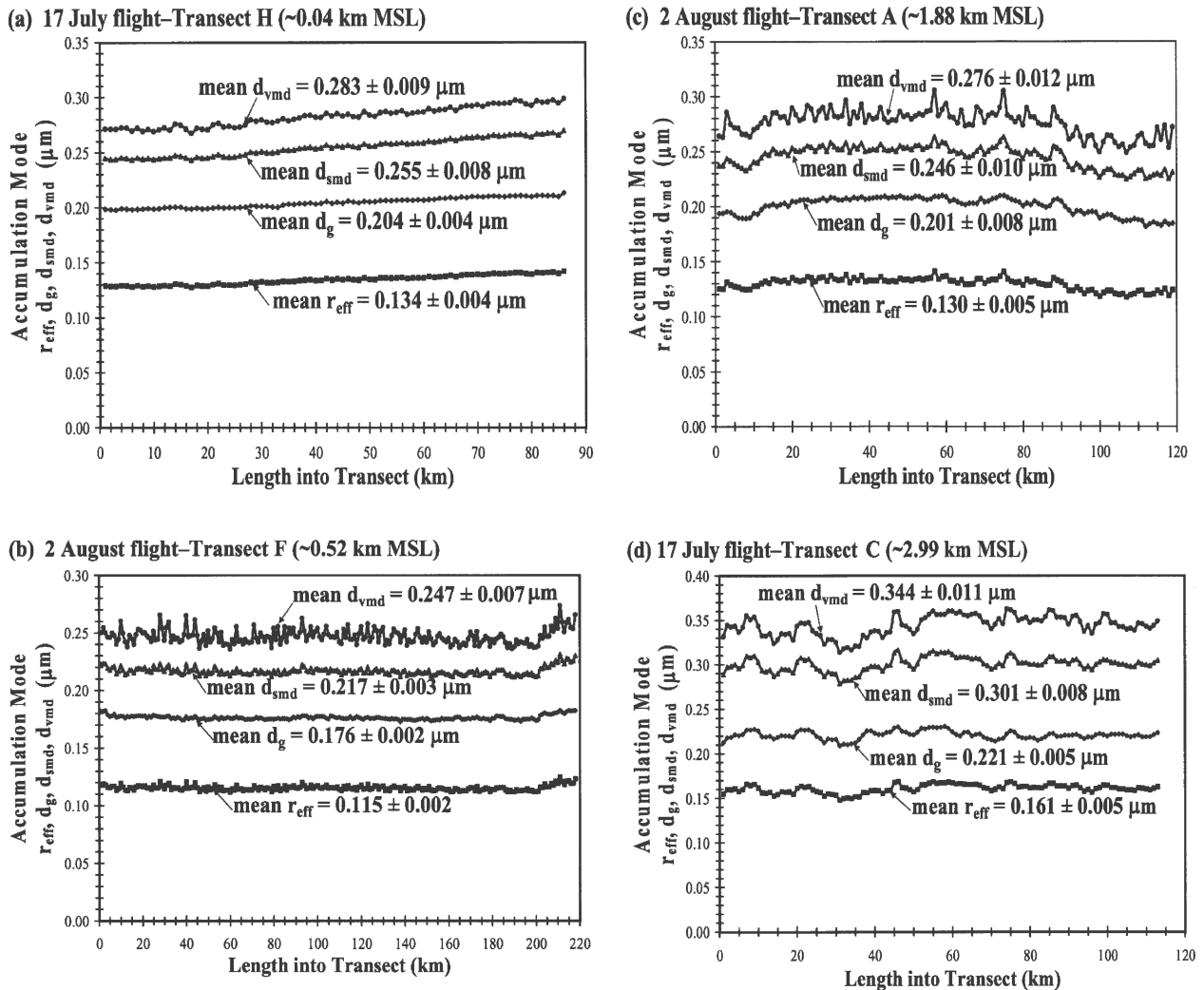To summarize, there was minimal horizontal vari-

FIG. 12. Small-scale (~1 km) horizontal variability of accumulation mode values of r_{eff}, D_g, D_{smd}, and D_{vmd} measured by the PCASP for selected transects of the 17 Jul and 2 Aug flights.

ability in particle size parameters associated with the accumulation mode on spatial scales of ~1 km. This is supported by the fact that in all transects of both flights, the standard deviation (SD) is no greater than 4%, and in 14 of 16 transects the SD ≤ 2%, of the mean size of the accumulation mode D_g. However, no conclusion can be drawn with regard to coarse-mode size variability since the number concentration of coarse-mode particles was so low throughout CLAMS.

4) PARTICLE NUMBER CONCENTRATIONS

Figure 13 shows the results from the autocorrelations for particle number concentration, N, as measured by the PCASP and TSI 3025A on 17 July and 2 August. All four panels show very high autocorrelation coefficient values above 0.985 when using a lag interval of 10 s, corresponding to a spatial resolution of ~1 km.

Therefore, we are confident that these data are free from instrument noise.

Since instrument noise is not a contributing factor to the variability in particle number concentration, we can look at Fig. 14 to illustrate the small-scale horizontal variability of particle number concentrations (N) measured over 0.1 μm < D_p < 4.0 μm by the PCASP and over 3 nm < D_p < ~1.0 μm by the TSI 3025A for selected transects at various levels of the atmosphere on both 17 July and 2 August. These transects also represent ~1-km variability in particle number concentration in the other transects not presented here. In all four transects shown, the PCASP and TSI 3025A capture most of the enhancements and declines in N quite accurately and consistently. Figure 14a is the near-surface example, showing a mean N value as measured by the PCASP of 341 ± 25 cm^{-3} (where the SD is 7%
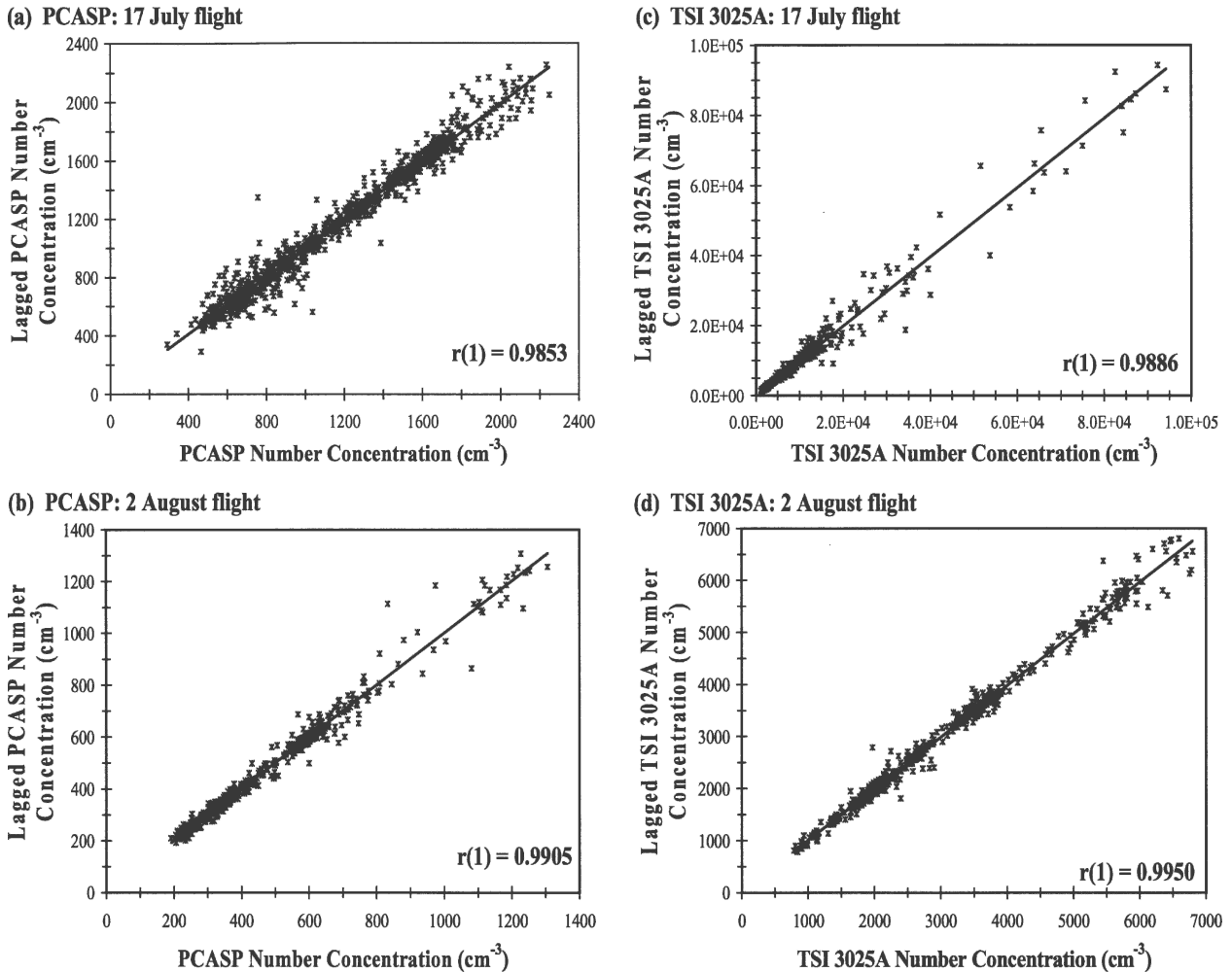
FIG. 13. Lag-1 autocorrelation for particle number concentration as measured by the PCASP [(a) 17 Jul and (b) 2 Aug] and TSI 3025A [(c) 17 Jul and (d) 2 Aug]. The lag is one measurement interval, which we have chosen to be 10-s or ~1-km resolution.

of the mean) and 5789 ± 567 cm^{-3} (SD is 10% of the mean) as detected by the TSI 3025A. Figure 14b shows a 218 km transect, the longest transect of either flight, at ~0.5 km MSL. Mean N values at this level derived from the PCASP were 389 ± 57 cm^{-3} (SD is 15% of the mean) and 2009 ± 244 cm^{-3} (SD is 12% of the mean) from the TSI 3025A. Figure 14d shows the N results for the highest transect flown on either day; the mean N value from the PCASP was 825 ± 150 cm^{-3} (SD is 18% of the mean) and 2045 ± 249 cm^{-3} (SD is 12% of the mean) from the TSI 3025A.

Perhaps the most interesting frame is Fig. 14c, which shows a leg of the 17 July flight that had a larger overland component than the other transects of these flights, which were mainly over the open ocean. There are two strong, localized enhancements in N, at $x \approx 25$ km and $x \approx 95$ km, that lead to the very large spread in N values discussed in section 3a(4). The first enhance-

ment occurs when the aircraft passed over the Great Dismal Swamp—a possible source of biogenic aerosols. The second, much larger, enhancement occurred when the Convair-580 flew over Norfolk, Virginia—the lone urban center in the region of study, and a source of urban/anthropogenic particles. Interestingly, the variability in N is much greater in the TSI 3025A data than in the PCASP data, indicating that these enhancements are mainly due to very small ($D_p < 0.1$ μm) nucleation or ultrafine mode aerosols.

In all four transects shown, as well as those not presented here, N values measured by the TSI 3025A were at least an order of magnitude greater than those from the PCASP. Given the different detection limits of these instruments, it is clear there is a strong dominance by particles having $D_p < 0.1$ μm at all levels of the lower troposphere. Furthermore, the variability in N has the lowest % SD near the surface, and grows con-
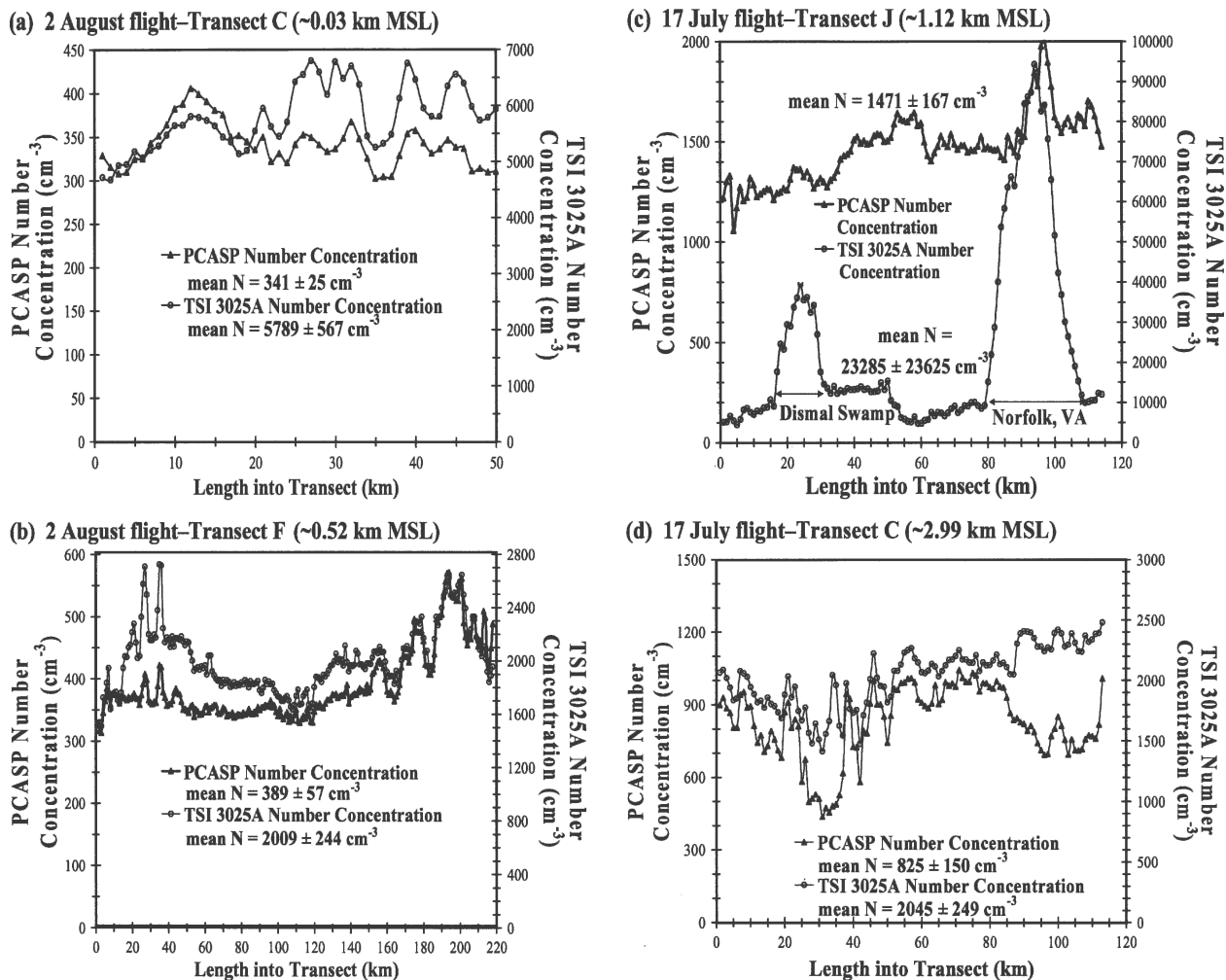
FIG. 14. Small-scale (~1 km) horizontal variability of particle number concentration, as measured by the TSI 3025A (open circles) and PCASP (closed triangles) for selected transects of the 17 Jul and 2 Aug flights.

sistently higher aloft. Finally, the horizontal variability in N can vary significantly on scales of ~1 km regardless of altitude, though the variability is obviously greatest when in close proximity to a strong source of particulate matter and/or precursor gases.

5) CONCLUSIONS REGARDING SMALL-SCALE VARIABILITY

Analysis of the small-scale horizontal variability of aerosol properties is needed to determine whether an average radiance in a given MISR scene can readily be translated into an average aerosol parameter over the scene, and whether the layer method employed in the particle size distributions is justified.

The resolution of the MISR aerosol retrieval algorithm is ~17.6 km. Therefore, an average radiance in a given scene represents the average aerosol parameter in that scene if that parameter varies minimally on a

horizontal scale of <15–20 km. Since ω_0, AOD and accumulation mode r_{eff} are the three aerosol parameters derived from MISR retrievals that are of most interest to the present study, we analyze their variability here. The ~4-km horizontal variability of ω_0 values derived from in situ measurements of σ_{sp} and σ_{apd} was quite small. Even on horizontal scales of 50–100 km, ω_0 varied less than the uncertainty associated with the MISR retrieval of ω_0, which is ~0.05 (Kahn et al. 1998). Therefore, the resolution of the MISR aerosol retrieval was sufficient to accurately detect any spatial variability in ω_0 during CLAMS. The analysis of the small-scale horizontal variability in AOD (Figs. 9 and 10) coupled with the results from Redemann et al. (2005) show that the variability in AATS-derived AOD is less than the uncertainty associated with the retrieval of AOD from MISR (0.05 or 20%, whichever is larger; Kahn et al. 2005). Thus, the resolution of the MISR retrieval is high

enough to capture any significant variability in AOD during CLAMS. The in situ measurements of accumulation mode r_{eff} show virtually no variability over horizontal scales of several hundred kilometers (Fig. 12); thus, the resolution of the MISR aerosol retrieval was sufficient to accurately detect any spatial variability in accumulation mode r_{eff} during CLAMS.

As discussed in section 3a(3), we used a layer analysis to determine particle size distributions. Grouping transects that were flown over horizontal scales of several hundred kilometers created the potential to introduce large spatial variability factors. The results presented in section 3b(3) and Fig. 12 show that, in fact, minimal variability was introduced using this layer method. As Fig. 12 illustrates, accumulation mode size parameter variability is remarkably low over horizontal scales of several hundred kilometers at all levels of the lower troposphere. Figures 11b,c,e,f illustrate the poor correlation between the "real time" and lagged coarse mode number concentration measurements. As a result, no conclusion can be made regarding the small-scale spatial variability of coarse mode size parameters since instrument noise accompanied measurements near the detection limit of the PCASP and FSSP-300. We see minimal horizontal variability in the relevant size parameters; thus, our methodology is justified.

c. Comparison of MISR retrievals with airborne in situ measurements

As discussed in section 2d, MISR categorizes aerosol columns into about a dozen broad classes, based on particle size, shape, and ω_0. MISR sensitivity to ω_0 is 2–4 groupings over the natural range of aerosol values; we can typically distinguish ~0.80 from ~0.88 from ~0.94 from ~1.0 (Kahn et al. 1998). These constraints are being updated and refined, as the validation process reflected by this and other studies progresses (e.g., Kahn et al. 2005). For example, Kalashnikova et al. (2005) demonstrated that MISR data can be used to distinguish randomly oriented spheres, ellipsoids, grains, and plates. The MISR retrievals in this paper are based on the early postlaunch MISR standard aerosol algorithm, version 12 (Martonchik et al. 1998).

Although the data available for optical property comparisons derived from Convair-580 and MISR measurements are limited, the available data from our in situ measurements allow for rigorous tests capable of disproving the MISR retrieval if it is erroneous. MISR retrieves column effective aerosol optical properties, whereas the ω_0 values derived from in situ measurements (Table 3) are averages of ω_0 throughout a prescribed vertical profile or horizontal transect. To make as accurate a comparison as possible between the in situ

and MISR results, we compare the MISR-retrieved values of ω_0 to the mean ω_0 values obtained during the largest profiles of each flight: profile 1 for 17 July and profile 2 for 2 August (Fig. 3). However, we need to account for horizontal and temporal offsets between MISR and the Convair-580, as well as aerosol above the top flight level of the aircraft. On both 17 July and 2 August, MISR flew over the region of study centered at 36.90° latitude, −75.71° longitude. The mean aircraft location during the spiral ascent of profile 1 on 17 July was 36.92° latitude, −75.71° longitude; the two platforms were virtually collocated. Similarly, the mean aircraft location for profile 2 on 2 August was 36.94° latitude, −75.78° longitude, so horizontal offsets between the two platforms are minimal, less than the 17.6-km resolution of the MISR aerosol retrieval algorithm. The MISR overpass occurred at 1608 UTC on both 17 July and 2 August. Profile 1 of the 17 July flight was flown from 1305–1337 UTC, so there is a temporal offset of ~3 h. On the 2 August flight, profile 2 was flown from 1626–1656 UTC—a temporal offset from the time of the MISR overpass of <1 h. AERONET data from the Chesapeake Lighthouse during these times show that particle size, AOD and ω_0 (though ω_0 data is unavailable for 2 August) varied minimally (<10%). Therefore, temporal offsets do not introduce significant uncertainties.

On 17 July, the total column 525 nm AOD measured with the AATS from ~0.10 km MSL, the lowest flight level of profile 1, was 0.408 ± 0.008. The AOD from the top of this profile to the top of the atmosphere was $0.012 \pm <0.001$, hence only ~3% of the AOD is unaccounted for in our vertical profile, so the mean ω_0 value from profile 1 on 17 July represents the total column aerosol quite well. On 2 August, the total column 525 nm AOD from ~0.05 km MSL, the base of profile 2, was 0.095 ± 0.001. The AOD from the top of this profile to the top of the atmosphere was $0.015 \pm <0.001$, thus ~16% of the AOD is unaccounted for in this profile, and for 2 August, a relatively larger amount of aerosol was unaccounted for by the in situ measurements. In summary, we are confident in directly comparing the in situ ω_0 values on 17 July with the column effective values derived from MISR, but the column-average ω_0 derived from the in situ measurements on 2 August has greater uncertainty.

The value of ω_0 at 550 nm using in situ data from the Convair-580 is 0.97 ± 0.01 for 17 July profile 1, whereas that derived from MISR measurements at 558 nm for the same time is >0.95. The in situ value of 550 nm ω_0 for 2 August profile 2 is 0.94 ± 0.03, and that derived from MISR measurements at 558 nm for the same time is 0.88 ± 0.05. For a more rigorous assessment of col-

umn-average ω_0 using our in situ data, we also performed a layer analysis similar to the one described in section 3a(3). Unlike the PCASP and FSSP-300, the nephelometer and PSAP were capable of obtaining accurate measurements in transects and profiles. Therefore, data from the profiles were included in the ω_0 layer analysis. The AOD-weighted total layer mean ω_0 for 17 July was 0.97 ± 0.01, and that for 2 August was 0.92 ± 0.02. Even with this secondary approach, there is some discrepancy in the remotely sensed versus in situ ω_0, particularly for 2 August. Although there is a significant amount of unaccounted aerosol above the top flight level on 2 August, a reasonable estimation of ω_0 for the upper tropospheric/stratospheric aerosol given the relative homogeneity of the atmosphere on this day would be 0.95 ± 0.05, so the cause of this difference between the MISR- and aircraft-derived total column ω_0 value on 2 August is unclear. Despite these differing ω_0 values, the SD for the MISR and in situ ω_0 overlap, so the MISR and in situ data show systematically higher ω_0 on 17 July than on 2 August, by about the same amount given measurement uncertainties. It should be noted that the in situ ω_0 values were measured at 550 nm, whereas the MISR effective wavelength is 558 nm. As discussed by Hartley et al. (2000), the values of ω_0 at these two wavelengths should not differ greatly.

In summary, the MISR results for 17 July and 2 August generally compare well with the in situ aerosol measurements obtained aboard the Convair-580. On 17 July, the MISR algorithm indicated "mostly small, spherical, clean" particles and on 2 August "small, spherical dirty" particles. The airborne in situ measurements show small particles on both days, with a r_{eff} of 0.14 μm from the PCASP compared to 0.12 μm from MISR on 17 July, and 0.12 μm from both the PCASP and MISR on 2 August. The lower ω_0 values found on 2 August support the MISR classification of the aerosol as "dirty" (i.e., more absorbing and, therefore, lower ω_0) versus the "clean" aerosol classification for the aerosol on 17 July when ω_0 values were higher. Table 8 summarizes the comparison between the MISR and Convair-580 results. It should be noted that the MISR retrievals were derived prior to analyzing the airborne data, and neither dataset was adjusted in any way.

4. Summary and conclusions

In this paper we summarize the optical properties and the size distributions of the aerosol measured aboard the UW's Convair-580 aircraft on 17 July and 2 August 2001 during the CLAMS field campaign over the East Coast of the United States. We have analyzed

TABLE 8. Comparison of aerosol parameters as determined by remotely sensed MISR retrievals and airborne in situ Convair-580 measurements during CLAMS.

Date (2001)	Parameter	MISR	Convair-580
17 Jul	AOD	0.38 ± 0.05 (558 nm)	0.40 ± 0.03 (525 nm)
	ω_0	>0.95 (558 nm)	0.97 ± 0.01 (550 nm)
	r_{eff}	0.12 (<+0.12/<−0.06) μm	0.14 ± 0.02 μm
	Classification	Small, spherical, clean	
2 Aug	AOD	0.10 ± 0.05 (558 nm)	0.09 ± 0.01 (525 nm)
	ω_0	0.88 ± 0.05 (558 nm)	0.94 ± 0.03 (550 nm)
	r_{eff}	0.12 (<+0.12/<−0.06) μm	0.12 ± 0.02 μm
	Classification	Small, spherical dirty	

small-scale horizontal variability in various aerosol parameters and compared the airborne in situ results with remote sensing measurements from MISR. Table 8 shows the results of the interplatform comparison.

Values of ω_0 at 550 nm were greater for all profiles and transects on 17 July than on 2 August; thus, we conclude the aerosol sampled on 17 July contained greater contributions from sulfate and possibly organic carbon particles. The particle composition measurements discussed by Magi et al. (2005) support this conclusion. Aerosol amount was significantly higher on 17 July than 2 August, in both the boundary layer and total column. We attribute this, in large part, to differing air parcel back trajectories on the two days. Particles with $D_p < 1.0$ μm predominated on both days, suggesting secondary aerosol production by processes such as gas-to-particle conversion.

Our analysis of the small-scale horizontal variability of several aerosol parameters revealed that ω_0, AOD and accumulation mode size varied minimally on scales of tens, and often times hundreds, of kilometers. Particle number concentration, however, exhibited significant spatial variability on scales as small as ~1 km. No conclusion could be made regarding the variability in coarse-mode size since the number concentrations of particles in this size range were so low ($\ll 1$ cm^{-3}).

In comparing the aerosol properties in CLAMS to those in TARFOX, we found that ω_0 at 550 nm and accumulation mode size were remarkably similar. However, significantly higher values of AOD and N were found in TARFOX. Particle composition differed, as well. In CLAMS, the aerosol was mainly composed of sulfate, whereas the aerosol in TARFOX was largely composed of carbonaceous compounds (Magi et al. 2005).

Our efforts at validating the aerosol retrievals from MISR with the in situ Convair-580 measurements showed that ω_0 values derived from MISR retrievals agree well with the in situ measurements on 17 July, and are within the error bars but not as close on 2 August, a much lower AOD case. The MISR retrievals classified the aerosol as small in size (i.e., $D_p < 0.7$ μm) on both days, which is in support of the size distribution measurements made in situ. Midvisible AOD values are in very good agreement, as well. The MISR retrieval detected both the similarities and the differences between aerosol properties measured on 17 July and 2 August.

Weather conditions during CLAMS were atypical for summer months along the East Coast of the United States: an unusual number of cold fronts, bringing deep northeasterly flows of cool, clean, dry air, traversed the region (Smith et al. 2005), producing uncharacteristically low pollution and aerosol optical depth values during the CLAMS campaign.

REFERENCES

Alam, A., J. P. Shi, and R. M. Harrison, 2003: Observations of new particle formation in urban air. *J. Geophys. Res.,* **108,** 4093–4109.

Anderson, T. L., and J. A. Ogren, 1998: Determining aerosol radiative properties using the TSI 3563 integrating nephelometer. *Aerosol Sci. Technol.,* **29,** 57–69.

——, and Coauthors, 1996: Performance characteristics of a high-sensitivity, three-wavelength, total scatter/backscatter nephelometer. *J. Atmos. Oceanic Technol.,* **13,** 967–986.

——, R. J. Charlson, D. M. Winker, J. A. Ogren, and K. Holmen, 2003: Mesoscale variations of tropospheric aerosols. *J. Atmos. Sci.,* **60,** 119–136.

Baumgardner, D., J. E. Dye, B. W. Gandrud, and R. G. Knollenberg, 1992: Interpretation of measurements made by the forward scattering spectrometer probe (FSSP-300) during the Airborne Arctic Stratospheric Expedition. *J. Geophys. Res.,* **97,** 8035–8046.

Birmili, W., A. Wiedensohler, J. Heintzenberg, and K. Lehmann, 2001: Atmospheric particle number size distribution in central Europe: Statistical relations to air masses and meteorology. *J. Geophys. Res.,* **106,** 32 005–32 018.

Bodhaine, B. A., 1995: Aerosol absorption measurements at Barrow, Mauna Loa and the South Pole. *J. Geophys. Res.,* **100,** 8967–8975.

Bond, T. C., T. L. Anderson, and D. Campbell, 1999: Calibration and intercomparison of filter-based measurements of visible light absorption by aerosols. *Aerosol Sci. Technol.,* **30,** 582–600.

Brook, J. R., and Coauthors, 1997: Temporal and spatial relationships in fine particle strong acidity, sulphate, PM_{10}, and $PM_{2.5}$ across multiple Canadian locations. *Atmos. Environ.,* **31,** 4223–4236.

Castanho, A. D. A., J. V. Martins, P. V. Hobbs, P. Artaxo, L. Remer, M. Yamasoe, and P. R. Colarco, 2005: Chemical characterization of aerosols on the East Coast of the United States using aircraft and ground-based stations during the CLAMS experiment. *J. Atmos. Sci.,* **62,** 934–946.

Covert, D. S., V. N. Kapustin, T. S. Bates, and P. K. Quinn, 1996: Physical properties of marine boundary layer particles of the mid-Pacific in relation to sources and meteorological transport. *J. Geophys. Res.,* **101,** 6919–6930.

Diner, D. J., and Coauthors, 1998: Multiangle Imaging Spectro-Radiometer (MISR) description and experiment overview. *IEEE Trans. Geosci. Remote Sens.,* **36,** 1072–1087.

Hartley, W. S., and P. V. Hobbs, 2001: An aerosol model and aerosol-induced changes in clear-sky albedo off the east coast of the United States. *J. Geophys. Res.,* **106,** 9733–9748.

——, P. V. Hobbs, J. L. Ross, P. B. Russell, and J. M. Livingston, 2000: Properties of aerosols aloft relevant to direct radiative forcing off the mid-Atlantic coast of the United States. *J. Geophys. Res.,* **105,** 9859–9885.

Hegg, D. A., and Y. J. Kaufman, 1998: Measurements of the relationship between submicron aerosol number and volume concentration. *J. Geophys. Res.,* **103,** 5671–5678.

——, J. Livingston, P. V. Hobbs, T. Novakov, and P. Russell, 1997: Chemical apportionment of aerosol column optical depth off the mid-Atlantic coast of the United States. *J. Geophys. Res.,* **102,** 25 293–25 303.

Hobbs, P. V., 1999: An overview of the University of Washington airborne measurements and results from the Tropospheric Aerosol Radiative Forcing Observational Experiment (TARFOX). *J. Geophys. Res.,* **104,** 2233–2238.

Hoppel, W. A., G. M. Frick, J. W. Fitzgerald, and R. E. Larson, 1994: Marine boundary layer measurements of new particle formation and the effects of nonprecipitating clouds have on aerosol size distribution. *J. Geophys. Res.,* **99,** 14 443–14 459.

Houghton, J. T., Y. Ding, D. J. Griggs, M. Nogner, P. J. van der Linden, and D. Xiaosu, Eds., 2001: *Climate Change 2001: The Scientific Basis.* Cambridge University Press, 892 pp.

Huebert, B. J., G. Lee, and W. L. Warren, 1990: Airborne aerosol inlet passing efficiency measurement. *J. Geophys. Res.,* **95,** 16 369–16 381.

Jaenicke, R., 1993: Tropospheric aerosols. *Aerosol–Cloud–Climate Interactions,* P. V. Hobbs, Ed., Academic Press, 1–31.

Kahn, R., P. Banerjee, D. McDonald, and D. Diner, 1998: Sensitivity of multiangle imaging to aerosol optical depth, and to pure-particle size distribution and composition over ocean. *J. Geophys. Res.,* **103,** 32 195–32 213.

——, ——, and ——, 2001: The sensitivity of multiangle imaging to natural mixtures of aerosols over ocean. *J. Geophys. Res.,* **106,** 18 219–18 238.

——, and Coauthors, 2004: Environmental snapshots from ACE-Asia. *J. Geophys. Res.,* **109,** D19S14, doi:10.1029/2003JD004339.

——, B. J. Gaitley, J. V. Martonchik, D. J. Diner, K. A. Crean, and B. Holben, 2005: Multiangle imaging spectroradiometer (MISR) global aerosol optical depth validation based on 2 years of coincident Aerosol Robotic Network (AERONET) observations. *J. Geophys. Res.,* **110,** D10S04, doi:10.1029/2004JD004706.

Kalashnikova, O. V., R. Kahn, I. N. Sokolik, and W.-H. Li, 2005: Ability of multiangle remote sensing observations to identify and distinguish mineral dust types: Optical models and retrievals of optically thick plumes. *J. Geophys. Res.,* **110,** D18S14, doi:10.1029/2004JD004550.

Kim, Y. J., and J. F. Boatman, 1990: Size calibration corrections for the Forward Scattering Spectrometer Probe (FSSP) for measurements of atmospheric aerosols of different refractive indices. *J. Atmos. Oceanic Technol.,* **7,** 681–688.

Kotchenruther, R. A., P. V. Hobbs, and D. A. Hegg, 1999: Humidification factors for atmospheric aerosols off the mid-Atlantic coast of the United States. *J. Geophys. Res.,* **104,** 2239–2251.

Li, J., J. D. G. Wong, J. S. Dobbie, and P. Chylek, 2001: Parameterization of the optical properties of sulfate aerosols. *J. Atmos. Sci.,* **58,** 193–209.

Liu, P. S. K., W. R. Leaitch, J. W. Strapp, and M. A. Wasey, 1992: Response of PMS airborne ASASP and PCASP to NaCl and latex particles. *Aerosol Sci. Technol.,* **16,** 83–95.

Magi, B. I., P. V. Hobbs, T. W. Kirchstetter, T. Novakov, D. A. Hegg, S. Gao, J. Redemann, and B. Schmid, 2005: Aerosol properties and chemical apportionment of the aerosol optical depth at locations off the U.S. East Coast in July and August 2001. *J. Atmos. Sci.,* **62,** 919–933.

Makela, J. M., I. K. Koponen, P. Aalto, and M. Kumala, 2000: One-year data of submicron size modes of tropospheric background aerosol in southern Finland. *J. Aerosol Sci.,* **31,** 595–611.

Martonchik, J. V., D. J. Diner, R. Kahn, M. M. Verstraete, B. Pinty, H. R. Gordon, and T. P. Ackerman, 1998: Techniques for the retrieval of aerosol properties over land and ocean using multiangle data. *IEEE Trans. Geosci. Remote Sens.,* **36,** 1212–1227.

——, K. Crean, and M. Bull, 2002: Regional aerosol retrieval results from MISR. *IEEE Trans. Geosci. Remote Sens.,* **40,** 1520–1531.

McMurry, P. H., 2000: A review of atmospheric aerosol measurements. *Atmos. Environ.,* **34,** 1959–1999.

Murphy, D. M., D. J. Cziczo, P. K. Hudson, M. E. Schein, and D. S. Thomson, 2004: Particle density inferred from simultaneous optical and aerodynamic diameters sorted by composition. *J. Aerosol Sci.,* **35,** 135–139.

Novakov, T., D. A. Hegg, and P. V. Hobbs, 1997: Airborne measurements of carbonaceous aerosols on the east coast of the United States. *J. Geophys. Res.,* **102,** 30 023–30 030.

Redemann, J., and Coauthors, 2005: Suborbital measurements of spectral aerosol optical depth and its variability at subsatellite grid scales in support of CLAMS 2001. *J. Atmos. Sci.,* **62,** 993–1007.

Reid, J. S., and P. V. Hobbs, 1998: Physical and optical properties of young smoke from individual biomass fires in Brazil. *J. Geophys. Res.,* **103,** 32 013–32 030.

Reist, P. C., 1993: *Aerosol Science and Technology*. 2d ed. McGraw-Hill, 379 pp.

Russell, P. B., and Coauthors, 1999: Aerosol-induced radiative flux changes off the United States mid-Atlantic coast: Comparison of values calculated from sunphotometer and *in situ* data with those measured by airborne pyranometer. *J. Geophys. Res.,* **104,** 2289–2307.

Schmid, B., and C. Wehrli, 1995: Comparison of sunphotometer calibration by Langley technique and standard lamp. *Appl. Opt.,* **34,** 4500–4512.

Seinfeld, J. H., and S. N. Pandis, 1998: *Atmospheric Chemistry and Physics: From Air Pollution to Climate Change*. John Wiley & Sons, 1326 pp.

Smirnov, A., B. N. Holben, O. Dubovik, N. T. O'Neill, L. A. Remer, T. F. Eck, I. Slutsker, and D. Savoie, 2000: Measurement of atmospheric optical parameters on U.S. Atlantic coast sites, ships, and Bermuda during TARFOX. *J. Geophys. Res.,* **105,** 9887–9901.

Smith, W. L., T. P. Charlock, R. Kahn, J. V. Martins, L. A. Remer, P. V. Hobbs, J. Redemann, and C. K. Rutledge, 2005: EOS *Terra* aerosol and radiative flux validation: An overview of the Chesapeake Lighthouse and Aircraft Measurements for Satellites (CLAMS) experiment. *J. Atmos. Sci.,* **62,** 903–918.

Stein, S. W., B. J. Gabrio, D. Oberreit, P. Hairston, P. B. Myrdal, and T. J. Beck, 2002: An evaluation of mass-weighted size distribution measurements with the Model 3320 aerodynamic particle sizer. *Aerosol Sci. Technol.,* **36,** 845–854.

Tanre, D., L. A. Remer, Y. J. Kaufman, S. Mattoo, P. V. Hobbs, J. M. Livingston, P. B. Russell, and A. Smirnov, 1999: Retrieval of aerosol optical thickness and size distribution over ocean from the MODIS airborne simulator during TARFOX. *J. Geophys. Res.,* **104,** 2261–2278.

van de Hulst, H. C., 1981: *Light Scattering by Small Particles*. Dover Publications, 470 pp.

Wang, J., and Coauthors, 2002: Clear-column radiative closure during ACE-Asia: Comparison of multiwavelength extinction derived from particle size and composition with results from Sun photometry. *J. Geophys. Res.,* **107,** 4688, doi:10.1029/2002JD002465.

Willeke, K., and P. A. Baron, Eds., 1993: *Aerosol Measurement: Principles, Techniques and Applications*. Van Nostrand Reinhold, 876 pp.